3D numerical modeling of mantle flow, crustal dynamics and magma genesis associated with slab roll-back and tearing: The eastern Mediterranean case

Armel Menant, Pietro Sternai, Laurent Jolivet, Laurent Guillou-Frottier, Taras Gerya

HAL Id: insu-01288706

https://insu.hal.science/insu-01288706

Submitted on 16 Mar 2016

1 3D numerical modeling of mantle flow, crustal dynamics and magma genesis associated with slab
2 roll-back and tearing: the eastern Mediterranean case
3

4 Armel Menant [a,b,c,d,]*, Pietro Sternai [e], Laurent Jolivet [a,b,c], Laurent Guillou-Frottier [b,a,c], Taras

5 Gerya [f]

6

7 [a] *Univ d'Orléans, ISTO, UMR 7327, 45071 Orléans, France*

8 [b] *BRGM, ISTO, UMR 7327, BP 36009, 45060 Orléans, France*

9 [c] *CNRS/INSU, ISTO, UMR 7327, 45071 Orléans, France*

10 [d] *Now at the Laboratoire des Fluides Complexes et leurs Réservoirs, Université de Pau et*

11 *des Pays de l'Adour, UMR 5150, Pau, France*

12 [e] *Department of Earth Sciences, University of Cambridge, Cambridge, UK*

13 [f] *Institute of Geophysics – Swiss Federal Institute of Technology (ETH), Zürich,*

14 *Switzerland*

15

16 ** Corresponding author: Armel Menant - Laboratoire des Fluides Complexes et leurs*

17 *Réservoirs*

18 *Université de Pau et des Pays de l'Adour*

19 *Avenue de l'Université – BP 1155 – 64013 PAU Cedex – France*

20 *(armel.menant@univ-pau.fr)*

Abstract

Interactions between subduction dynamics and magma genesis have been intensely investigated, resulting in several conceptual models derived from geological, geochemical and geophysical data. To provide physico-chemical constraints on these conceptual models, self-consistent numerical simulations containing testable thermo-mechanical parameters are required, especially considering the three-dimensional (3D) natural complexity of subduction systems. Here, we use a 3D high-resolution petrological and thermo-mechanical numerical model to quantify the relative contribution of oceanic and continental subduction/collision, slab roll-back and tearing to magma genesis and transport processes. Our modeling results suggest that the space and time distribution and composition of magmas in the overriding plate is controlled by the 3D slab dynamics and related asthenospheric flow. Moreover, the decrease of the bulk lithospheric strength induced by mantle- and crust-derived magmas promotes the propagation of strike-slip and extensional fault zones through the overriding crust as response to slab roll-back and continental collision. Reduction of the lithosphere/asthenosphere rheological contrast by lithospheric weakening also favors the transmission of velocities from the flowing mantle to the crust. Similarities between our modeling results and the late Cenozoic tectonic and magmatic evolution across the eastern Mediterranean region suggest an efficient control of mantle flow on the magmatic activity in this region, which in turn promotes lithospheric deformation by mantle drag via melt-induced weakening effects.

2

1.   Introduction

Arc magmatism is one of the most typical surface expressions of subduction dynamics tracking physico-chemical processes from the upper mantle to the crust [*Arculus*, 1994]. It is broadly accepted that the genesis of these magmas is dominated by partial melting of a hydrated mantle wedge source, as the result of the H_2O release from the subducting oceanic lithosphere [*Arculus*, 1994; *Grove et al.*, 2006]. These primary mafic magmas then ascend through the mantle, reaching the base of the overriding crust where they can be retained in the melting assimilation storage and homogenization (MASH) zone [*Hildreth and Moorbath*, 1988]. During their storage and their subsequent ascent up to the upper crust, these magmas undergo some degrees of fractionation and crustal assimilation, which provide the typical calc-alkaline magmatic trend. To reach a coherent understanding of the interactions between subduction dynamics and magma genesis, numerical experiments have been performed involving mechanical, thermal and petrological constraints [*Huw Davies and von Blanckenburg*, 1995; *Nikolaeva et al.*, 2008; *Zhu et al.*, 2009, 2013; *Gerya and Meilick*, 2011; *Bouilhol et al.*, 2015]. However, in subduction environment involving slab roll-back and tearing, the 3D effects of slab dynamics and related asthenospheric flow on the three-dimensional (3D) space and time distribution and composition of magmas have been most often assessed by conceptual models [e.g. *Pe-Piper and Piper*, 2006; *Dilek and Altunkaynak*, 2009; *Ersoy and Palmer*, 2013; *Jolivet et al.*, 2015].

In 3D oceanic-continental subduction system involving slab roll-back and tearing, particular attention has been given to the control of subduction dynamics and related asthenospheric flow on lithospheric deformation without considering the role of magmatic processes [*Jadamec and Billen*, 2010; *Li et al.*, 2013; *Capitanio*, 2014; *Duretz et al.*, 2014; *Magni et al.*, 2014; *Sternai et al.*, 2014]. Rheological weakening effect of magmas resulting from the partial melting of the upper mantle and the crust has, however, major consequences

70   on lithospheric-scale tectonics [*Gerya and Meilick*, 2011], which need to be tested across

71   complex 3D subduction system.

72   Here we use a 3D high-resolution petrological and thermo-mechanical numerical

73   geodynamic model to assess (1) the role of subduction dynamics involving slab roll-back and

74   tearing processes on the magmatic activity within the overriding lithosphere and (2) the

75   weakening effect of magmas on the lithospheric deformation. The numerical setup accounts

76   for experimentally calibrated non-Newtonian visco-plastic rheologies and physico-chemical

77   processes, such as slab dehydration, fluid transport, partial melting, melt extraction and

78   crustal growth [e.g. *Nikolaeva et al.*, 2008; *Zhu et al.*, 2013]. Modeling results suggest that

79   slab dynamics and related asthenospheric flow affect the genesis, transport and emplacement

80   of magmatic bodies both in the arc and back-arc domain and that such melts weaken the

81   lithosphere, promoting lithospheric deformation and its coupling with asthenospheric flow.

82   Our results are then compared to observations from the eastern Mediterranean region, where

83   the late Cenozoic evolution of the subduction zone including slab roll-back and tearing

84   processes and associated magmatism is relatively well constrained (Fig. 1) [e.g. *Jolivet and*

85   *Faccenna*, 2000; *Pe-Piper and Piper*, 2006; *Dilek and Altunkaynak*, 2009; *Ersoy and Palmer*,

86   2013; *Jolivet et al.*, 2013].

87

88   **2.   Late Cenozoic evolution of the eastern Mediterranean subduction zone**

89   Since the Mesozoic, the geodynamic evolution of the Mediterranean realm is characterized

90   by the subduction and/or collision of successive oceanic and continental lithospheres,

91   governed by the Africa-Eurasia convergence [*Stampfli and Borel*, 2002; *Menant et al.*, 2016].

92   Since the latest Eocene-early Oligocene (i.e. 35-30 Ma), increasing rate of slab retreat has

93   resulted in the opening of back-arc basins, such as in the eastern Mediterranean region where

94   the Hellenic southward slab roll-back led to the opening of the Aegean domain [*Jolivet and*

95 *Faccenna*, 2000]. In this extensional context, medium- to high-temperature rocks were

96 exhumed as several metamorphic core complexes (MCCs), such as in the Rhodope massif, the

97 Cyclades and the Menderes massif (Fig. 1) [*Lister et al.*, 1984; *Bozkurt and Oberhänsli*, 2001;

98 *Vanderhaeghe*, 2004; *Brun and Sokoutis*, 2007; *Jolivet et al.*, 2013]. At the same time,

99 subduction and collision of the Arabian plate with the southern margin of the Tauride belt

100 took place further east (Fig. 1c) [*Jolivet and Faccenna*, 2000]. The present-day kinematics of

101 this region is characterized by an overall counterclockwise rotation of the surface velocity

102 vectors as recorded by GPS measurements (Fig. 2a) [*Reilinger et al.*, 2006; *Le Pichon and*

103 *Kreemer*, 2010] controlled by the westward extrusion of Anatolia, which is mainly

104 accommodated by the North Anatolian Fault (NAF) [*Şengör et al.*, 2005].

105   At ~150 km-depth, tomographic models for the eastern Mediterranean region show trench-

106 parallel variations in seismic velocity, with low-velocity anomalies located in eastern and

107 western Anatolia and interpreted as major break-off or tears in the slab that displays a high-

108 velocity anomaly (see star symbols in Fig. 2b) [*de Boorder et al.*, 1998; *Wortel and Spakman*,

109 2000; *Li et al.*, 2008]. The complex geometry of the subducting lithosphere thus resulted in a

110 complex mantle convection pattern including both poloidal and toroidal flows [*Faccenna and*

111 *Becker*, 2010], the latter having been partly imaged by *SKS* splitting anisotropy (Fig. 2b)

112 [*Paul et al.*, 2014].

113   Integrated in this complex tectonic frame, magmatic occurrences show a specific spatial

114 and temporal distribution associated with variable petrological and geochemical composition

115 [*Menant et al.*, 2016]. Since the Oligocene (i.e. 34-23 Ma), high-potassic calc-alkaline to

116 shoshonitic magmatism was progressively emplaced southward from the Rhodope massif to

117 the Cyclades and the Menderes massif, associated with the exhumation of MCCs (Figs. 1a, c)

118 [*Pe-Piper and Piper*, 2006; *Dilek and Altunkaynak*, 2009; *Ersoy and Palmer*, 2013]. In

119 addition to this first-order migration, a secondary southwestward migration of the magmatic

120 activity is recorded during the Miocene (i.e. 23-5 Ma) from the Menderes massif to the

121 Cyclades (Fig. 1a) [*Jolivet et al.*, 2015]. Evolution of geochemical and isotopic composition

122 of this magmatism suggests an increase of mantle source component relative to the crustal

123 source component [*Keskin*, 2003; *Dilek and Altunkaynak*, 2009; *Ersoy and Palmer*, 2013;

124 *Jolivet et al.*, 2015], finally producing alkaline magmas with a major depleted asthenospheric

125 source component [*Ersoy and Palmer*, 2013]. In eastern Anatolia, a wide late Miocene-

126 Quaternary volcanic province was also emplaced with composition evolving from high-

127 potassic calc-alkaline to alkaline (Fig. 1c) [*Keskin*, 2003].

128

129 **3.   Numerical modeling**

130   In this section we describe the modeling approach and the initial reference model setup and

131 then outline the main objectives of the parametric study.

132

133 *3.1.   Modeling approach and setup*

134   We use the wealth of observations from the eastern Mediterranean region to design and

135 calibrate numerical experiments that could be qualitatively and quantitatively compared to the

136 first order evolution of this region during the late Cenozoic. We stress, however, that the main

137 objective of our work is to investigate the 3D effects of slab retreat and tearing on magmatism

138 and we do not claim that our models provide an exhaustive description of geodynamics across

139 the area. As such, results may also be representative of other regions similarly characterized

140 by fast evolving narrow subduction zones involving lateral variations of the subducting

141 material (e.g. central and western Mediterranean region, southeastern Asia).

142   Numerical modeling was performed using the code *I3ELVIS*, like in other recent studies

143 [*Zhu et al.*, 2009, 2013; *Li et al.*, 2013; *Duretz et al.*, 2014; *Sternai et al.*, 2014]. The code

144 solves the mass, momentum and heat conservation equations based on a conservative finite-

145 difference scheme combined with a marker-in-cell technique and includes non-Newtonian

146 visco-plastic rheologies (Table S1) [*Gerya and Yuen*, 2007]. In addition, this code accounts

147 for physico-chemical processes, such as slab dehydration, fluid transport, partial melting, melt

148 extraction and crustal growth at continental margin [*Zhu et al.*, 2013]. Details on the

149 numerical approach and material properties used in our numerical experiments are available

150 as Supplementary Material.

151   In all our experiments, the model domain measures $1500 \times 680 \times 656$ km in the *x*, *y* and *z*

152 directions, respectively, resolved by $437 \times 277 \times 149$ grid nodes giving a resolution of $3.4 \times$

153 2.5×4.4 km (Fig. 3a). Around 130 million additional randomly distributed markers are used

154 for advecting the material properties and computing water release, transport and consumption

155 as well as partial melting and melt extraction. The initial setup is designed with an overriding

156 continental lithosphere and a subducting oceanic lithosphere including a small continent (i.e.

157 500×328 km in *x* and *z* directions, respectively), which represent the Eurasian plate and the

158 converging Mesogean and Arabian lithospheres, respectively (Figs. 1c and 3a). A 10 km thick

159 trench-parallel weak zone is prescribed at the interface between the overriding and subducting

160 lithospheres in order to initiate subduction. In our reference model, the overriding continental

161 lithosphere is composed by 30 km and 20 km thick upper and lower crust, respectively, while

162 the subducting continental crust is composed of 20 km and 10 km thick upper and lower crust,

163 respectively (Figs. 3a and 3b). The initial thermal structure of the continents is laterally

164 uniform and varies for each experiment (see *Section 3.2*). In the reference model, this is a

165 linear vertical gradient with 0 °C at the surface and 1300 °C at 89 km and 98 km depth for the

166 overriding and subducting continental lithospheres, respectively. The oceanic lithosphere

167 incorporates a 3 km thick hydrated basaltic crust and a 5 km thick gabbroic crust and its

168 thermal structure, also different for each experiment, is defined using a half-space cooling age

169 (of 60 Ma for the reference model) [*Turcotte and Schubert*, 2002]. These lithospheres overlay

170   an asthenospheric mantle characterized by an initial adiabatic temperature gradient of ~0.5 °C

171   km^{-1}.

172   Velocity boundary conditions are free slip at both back and front boundaries ($z = 0$ and $z = $

173   656 km). Material influx is imposed through the right and left boundaries ($x = 0$ and $x = 1500$

174   km). Velocities across these boundaries are null except for the first 250 km depth of the right

175   boundary where a ~1.9 cm yr^{-1} influx is applied (Fig. 3a), scaled on the African plate absolute

176   motion estimated between 1.2 and 2.5 cm yr^{-1} since the Oligocene [*Jolivet and Faccenna*,

177   2000]. The mass conservation is then ensured by material outflux through the upper and lower

178   permeable boundaries ($y = 0$ and $y = 680$ km). The top surface of the lithosphere is calculated

179   dynamically as an internal free surface by using an initial 12-15 km thick low-viscosity layer

180   simulating either air (for $y < 12$ km) or sea water. The large viscosity contrast caused by this

181   low-viscosity layer minimizes shear stresses at the top of the lithospheres that effectively

182   approximates a free surface [*Schmeling et al.*, 2008].

183

184   *3.2.   Parametric study on lithospheric geothermal gradient and rheological layering*

185   To assess the role of subduction dynamics on magma genesis and transport, we explore a

186   wide range of rheological profiles of interacting continental and oceanic plates by changing

187   their thermal gradients (Table S2). In addition, since there is no consensus on the rheological

188   structure of the lithosphere, especially in the eastern Mediterranean region whose

189   geodynamical history is long and complex, different rheological layering have been tested for

190   the continental lithospheres by defining either one or two crustal layers characterized by

191   distinct non-Newtonian rheologies (Figs. 3a and b). We thereby control the overall

192   rheological contrast and therefore the degree of plate coupling between the interacting

193   lithospheres in our experiments [*Gerya and Meilick*, 2011] leading to reproduce different

194   regimes of subduction with either advancing or retreating trench. Changing the lithospheric

195   thermal gradients also modifies the degree of partial melting of the lithosphere, allowing us to

196   investigate the weakening effect of magmas on lithospheric deformation. In the following, we

197   use acronyms like *2c89-60* for model with two-layer continental crust, an overriding

198   lithosphere 1300 °C isotherm at 89 km depth and 60-Myr old oceanic lithosphere (Fig. 3a).

199

200   **4.   Results**

201   In this section, we outline the main numerical results through a series of figures obtained

202   from selected experiments (Table S2) focusing on the overall evolution of these models, on

203   the resulting asthenospheric and lithospheric flow pattern and on the genesis and evolution of

204   partially molten rocks from the mantle to the crust. Figs. 4 and 5 illustrate the evolution of

205   models *2c89-60* and *1c113-70*, characterized by two- and one-layer continental crust,

206   respectively. Fig. 6 shows the temporal variations of the velocity of trench migration from

207   selected experiments and from kinematic reconstructions of the eastern Mediterranean region

208   [*Menant et al.*, 2016]. Fig. 7 highlights the mantle and crustal flow pattern and the strain rate

209   distribution in the overriding lithosphere from selected models. Finally, Figs. 8 and 9 illustrate

210   the temporal distribution of partially molten rocks from models *2c89-60* and *1c113-70*.

211   Additional results are also described in this section, although related figures are available as

212   Supplementary Material.

213

214   *4.1.   Succession of events: oceanic and continental subduction followed by slab tearing*

215   In our reference model *2c89-60* (Fig. 4; Videos S1 and S2), subduction initiates through

216   progressive bending and roll-back of the oceanic slab, associated with a homogeneous

217   stretching of the overriding continental lithosphere (Fig. 4a). Subsequent continental

218   subduction then induces along-trench buoyancy variations resulting in progressive curvature

219   of the trench (Fig. 4b). When the continental slab reaches ~150 km depth, trench-parallel

220 tearing occurs at the transition between the more buoyant continental lithosphere and the

221 oceanic lithosphere (Fig. 4b). The slab tear then propagates along this compositional

222 boundary inducing trench-perpendicular tearing (Fig. 4c). Once decoupled from the oceanic

223 lithosphere, the torn continent bends up and collides into the overriding plate while the still

224 active oceanic subduction zone continues to retreat associated with slab flattening. This

225 succession of events is robust through all experiments with two-layer continental crust (model

226 *2c84-100* with higher lithospheric thermal gradient; Fig. S1), except when the lithospheric

227 thermal gradient is low, which leads to overall compression in the overriding lithosphere

228 (model *2c98-100*; Fig. S2a). This transient evolution is also consistent in models with one-

229 layer continental crust (model *1c113-70*; Fig. 5; Videos S3 and S4) with the exception of a

230 higher stretching of the subducting continental lithosphere also associated with crustal

231 decoupling, which thus delays slab tearing (Figs. 5b and c). It is noteworthy that the apparent

232 lack of lithospheric mantle below the overriding stretched continental crust (model *1c113-70*;

233 Fig. 5) does not imply that the crust lies directly on the asthenosphere. Depending on the

234 evolution of the thermo-mechanical properties of the peridotite, the lithosphere-asthenosphere

235 boundary is therefore more accurately defined in our experiments by considering the 1200 °C

236 isotherm (Fig. 3b).

237   In all numerical experiments, laterally varying subduction dynamics exerts a major control

238 on the surface kinematics. Coeval subduction of oceanic and continental lithospheres results

239 in an along-trench variation of the rate of trench retreat evolving in the reference model *2c89-*

240 *60* from ~2 cm yr^{-1} to 3-6 cm yr^{-1} above the continental and oceanic slab, respectively (Fig.

241 6a). Once slab tearing has occurred, trench retreat accelerates above the continuing oceanic

242 subduction zone reaching up to ~6 cm yr^{-1} in this model. Models with higher lithospheric

243 thermal gradient show a sensibly faster trench retreat (model *2c84-100*; ~9 cm yr^{-1}), while

244 those with a lower lithospheric thermal gradient are characterized by a slowly advancing

245 oceanic trench (model *2c98-100*; 0.5-2 cm yr^{-1}; Fig. 6b). Finally, models with one-layer

246 continental crust (model *1c113-70*) also show faster trench retreat than the reference model

247 despite a lower lithospheric thermal gradient (reaching up to ~7 cm yr^{-1} above the fast

248 retreating oceanic slab; Fig. 6c). The magnitude of these trench velocities is broadly similar to

249 the rate of trench retreat for the Hellenic subduction system, estimated between 0.5 and 3

250 cm yr^{-1} during the late Cenozoic (see solid line in Fig. 6d) [*Menant et al.*, 2016].

251

252 *4.2.   Asthenospheric vs. lithospheric flow pattern*

253 Except for model *2c98-100* characterized by major compressional tectonics (Fig. S2), all

254 performed numerical experiments show an initial dominant poloidal asthenospheric flow,

255 initiated at the slab tip and upwelling into the mantle wedge (Fig. 7a). When slab tearing

256 occurs, the asthenospheric flow changes to a poloidal flow coming through the newly formed

257 slab windows then evolving in a toroidal flow, which finally reaches the mantle wedge (Fig.

258 7b). Meanwhile, extrusion of the overriding lithosphere towards the oceanic subduction

259 occurs (Figs. 4c and 5c). Extrusion tectonics in models with two-layer continental crust takes

260 place in a restricted zone above the trench-perpendicular slab tear, where the deformation is

261 localized along a strike-slip fault zone (Fig. 7c). Lithospheric and asthenospheric flows in the

262 extensional back-arc domain are then sub-parallel and controlled by the slab roll-back (Fig.

263 7d). However, the horizontal component of flow velocity at the lithosphere-asthenosphere

264 boundary is subject to an abrupt decrease (see velocity profile in inset of Fig. 7c). Conversely,

265 models with one-layer continental crust are characterized by more pronounced strike-slip

266 faulting during upper plate extrusion reaching a wide extensional region above the fast

267 retreating oceanic slab (Fig. 7e). In addition, the comparatively weaker continental lithosphere

268 in this extensional domain allows for more efficient transmission of the asthenospheric flow

269 to the overriding lithosphere, as shown by a progressive decrease of the horizontal component

11

270   of flow velocity from the asthenosphere to the upper part of the continental crust (see velocity

271   profile in inset of Fig. 7e).

272

273   *4.3.   Genesis and transport of partially molten rocks*

274   In our reference model *2c89-60* (Fig. 8), the first stage of oceanic subduction is associated

275   with (1) partial melting of the lower continental crust of the overriding lithosphere (Figs. 8a

276   and c) and (2) water release from the hydrated subducting oceanic crust at ~70 km depth

277   (Fig. 8d). Subsequent hydration of the mantle wedge contributes to its partial melting

278   resulting in a wave-like plume geometry of partially molten mantle (according to the

279   magmatic plume description of *Zhu et al.* [2009]) that starts to ascend at ~150 km depth (Figs.

280   4a and 8d). While the oceanic slab retreats, partially molten crust and mantle are stored at the

281   base of the overriding crust, being passively transferred from the arc to the back-arc domain

282   through time (see vertical cross-sections in Fig. 8). The up-bending of the subducting

283   continental lithosphere resulting from slab tearing is accompanied by fast rising and storage of

284   partially molten mantle and continental crust as well as of dry asthenosphere below the active

285   collision zone (Figs. 8e and h). A significant amount of partially molten sediments is then

286   added to the stacked material, which is laterally transferred through the collision zone into the

287   back-arc domain and exhumed through the stretching crust up to the surface (Figs. 8i and k).

288   Lateral migration of partially molten mantle at the base of the stretched crust above the

289   ongoing subduction zone also takes place (Fig. 8e) and is progressively replaced by dry

290   asthenosphere (Fig. 8i).

291   In model *2c98*-100 displaying slow subduction associated with a compressional regime

292   (Figs. S2b and c), the magmatic activity is restricted to small amounts of partially molten

293   continental crust and sediments slowly ascending within the thickening overriding

294   lithosphere. In model *2c84-100* characterized by two-layer continental crust and fast slab roll-

295 back (Fig. S1), the hydrated and partially molten rocks evolution is faster, similar to the

296 reference model *2c89-60*, except that the wave-like plume of partially molten mantle in the

297 mantle wedge develops later (Fig. S3). Finally, the magmatic evolution of model *1c113-70*

298 with one-layer continental crust shows a number of differences. (1) A major partial melting

299 event occurs at the base of the overriding crust (Fig. 5). The partially molten material is then

300 progressively exhumed through the stretched crust forming a high temperature dome-like

301 structure (Figs. 9a, c and j). (2) The ascent of partially molten mantle in the mantle wedge

302 starts deeper, from ~300 km depth (Fig. 5a) and occurs as a wave-like plume (Fig. 5b), except

303 around the torn continental slab where it ascends as regularly-spaced finger-like plumes (Fig.

304 5c). (3) The long residence time of continental slab at depth before tearing results in

305 increasing partial melting of the crust and subsequently finger-like upwelling of melts

306 (Fig. 9g).

307

308 **5.   Discussion**

309   We discuss below the relationships between magmatism, mantle flow and lithospheric

310 deformation assuming that partially molten rocks mimic magmatic sources from which

311 magmas with specific composition are potentially extracted. Finally, we compare our results

312 to observations from the eastern Mediterranean region.

313

314 *5.1.   Ascent of partially molten mantle*

315   During the initial subduction of the oceanic lithosphere, slab dehydration and subsequent

316 hydrated partial melting result in the accumulation of mantle-derived melts within the mantle

317 wedge [*Grove et al.*, 2006]. According to our models, partially molten mantle with lower

318 viscosity and density rises up as plumes (Figs. 8b and 9b). This ascent is controlled by the

319 competition between the buoyancy of partially molten rocks and the subduction drag

320 (depending on viscosity and slab dip). The predominance of the buoyancy force results in the

321 development of Rayleigh-Taylor instabilities at the interface between hydrated/partially

322 molten mantle and dry mantle, initiating plume rising. *Zhu et al.* [2013] suggest that plate

323 convergence rate affects the depth of the plume growth with faster plate convergence (i.e.

324 ~6.5 cm yr^{-1}) carrying more efficiently the hydrated oceanic crust down the subduction zone

325 than slower plate convergence (i.e. ~2 cm yr^{-1}). We can add upon this evidence that the

326 asthenospheric flow related to slab roll-back and tearing is another crucial process affecting

327 the initiation and trajectories of partially molten rock upwelling through the mantle wedge.

328 Indeed, as soon as subduction and subsequent partial melting of the hydrated mantle start, a

329 sub-horizontal asthenospheric flow develops in the mantle wedge as a result of the dominant

330 poloidal flow component initiated at the slab tip (~5 cm yr^{-1}; model *2c89-60*; Figs. 8d and

331 10a). This sub-horizontal asthenospheric flow, particularly fast for high rate of slab roll-back,

332 is then deflected downward close to the slab-mantle interface (~10 cm yr^{-1}; model *1c113-70*,

333 Figs. 9d and 10b) resulting in an asthenospheric return flow that tends to delay the growth of

334 the plumes (initiated ~300 km depth in model *1c113-70*, Fig. 5a). Conversely, slab roll-back

335 and tearing promotes an asthenospheric upwelling which drags upward partially molten rocks

336 in the mantle wedge (Figs. 8k and 9k). In our experiments, this magmatic source mainly

337 ascends as wave-like plumes (Figs. 4b and 5b) but also as finger-like plumes, especially close

338 to the torn continental slab (model *1c113-70*, Figs. 5b and c). *Zhu et al.* [2009] argued that the

339 main controlling factor on the geometry of these plumes is the viscosity variation of the

340 partially molten material. In this study, the constant viscosity of 10^{19} Pa s for these partially

341 molten phases (constrained by imposing a lower cut-off value for viscosities in our

342 experiments, see Supplementary Material) suggests that other factors also control the plume

343 structure in the mantle wedge. We find here that finger-like plumes initiate above a steep and

344 slow sinking slab associated with slow asthenospheric return flow (Fig. 9h; ~1.6 cm yr^{-1}),

345 when the continental slab buoyancy force counterbalances the slab pull force. The reduced

346 stress imposed by this slow asthenospheric flow then promotes the development of along-

347 trench Rayleigh-Taylor instabilities at the slab-mantle interface enabling the growth of finger-

348 like plumes. Conversely, in the case of fast retreating slab (Figs. 8j and 9j), related faster

349 asthenospheric flow (i.e. ~6 cm yr^{-1}) avoids the initiation of these along-trench Rayleigh-

350 Taylor instabilities resulting in the ascent of partially molten rocks as a wave-like plume.

351

352 *5.2. Magmatic evolution in the lower crust and mantle flow*

353 Besides controlling the ascending trajectories of magmatic sources through the mantle

354 wedge, the dominant toroidal asthenospheric flow related to slab tearing (Figs. 10c and d)

355 drives the trench-parallel migration of magmas and their emplacement at the base of the

356 overriding continental crust. Here, both partially molten mantle and crust are stored during the

357 first stage of subduction (Figs. 8 and 9) with a predominance of crustal-derived magmas,

358 especially in model *1c113-70* where the prescribed one-layer continental crust is less

359 refractory than the two-layer continental crust defined in model *2c89-60*. When slab tearing

360 occurs, large amount of both partially molten crust and mantle are stored at the base of the

361 overriding crust (Figs. 8e and 9e). Subsequent toroidal asthenospheric flow due to protracted

362 roll-back of the oceanic slab then drags these magmatic sources from the collision zone to the

363 back-arc domain, above the retreating subduction (Figs. 10c and d). In addition, we found a

364 lateral increase of mantle-derived relative to crust-derived melts in the back-arc domain (Fig.

365 5e) and a final upwelling of hot and dry asthenosphere potentially resulting in the adiabatic

366 melting of depleted mantle, which is not considered in the model (Figs. 8i and 9i).

367 Implementation of this magmatic process should be therefore a major improvement for future

368 works in order to discuss the control of asthenospheric upwelling on the genesis of magmas

369 with alkaline composition in the back-arc domain.

370   No significant contribution from partial melting of the oceanic crust was recognized in our

371   experiments, in turn suggesting that most magmas within the mantle wedge are generated

372   from hydrated mantle, even in warm subduction zones [*Bouilhol et al.*, 2015]. In the MASH

373   zone, mantle- and crustal-derived magmas may mix and therefore change composition, as if

374   they undergo fractionation and crustal assimilation processes [*Hildreth and Moorbath*, 1988].

375   Sedimentary material likely contributes to the maturation of these magmas in the MASH

376   zone, especially across continental subduction zone where the strong coupling of the

377   continental lithospheres enhances the basal erosion of the upper plate along the subduction

378   interface and therefore the burial of detrital continental crust (Figs. 8i and k).

379

380   *5.3.   Magmatism and lithospheric deformation*

381   Low-viscosity partially molten rocks stored in the overriding lithosphere allow for

382   decreasing the bulk strength of the upper plate [*Watts and Burov*, 2003] thus favoring partial

383   decoupling between the continental crust and the underlying lithospheric mantle (Figs. 9b and

384   f). This melt-induced lithospheric weakening also enhances the decoupling at the subduction

385   interface, which in turn increases the rate of slab roll-back, thereby affecting lateral extrusion

386   and stretching of the upper plate (Fig. 7; comparison between slow evolving models *2c89-60*

387   and *2c98-100* and fast evolving models *1c113-70* and *2c84-100*).

388   In our experiments, low-viscosity partially molten rocks exhumed through the overriding

389   crust also provide a strong rheological contrast with the surrounding high-viscosity rocks

390   (Figs. 8b and 9b) affecting the distribution of crustal deformation. Strike-slip faulting and

391   back-arc-related intense lithospheric stretching thus localize in the weaker parts of the crust

392   accommodating the lateral extrusion of continental block and fast slab roll-back, respectively

393   (model *2c89-60*; Fig. 7c). Moreover, in accordance with previous studies [*Gerya and Meilick*,

394   2011; *Capitanio*, 2014], our experiments show that a large amount of partial melting of the

395 overriding crust decreases the bulk lithospheric strength and favors the propagation of the

396 strike-slip fault zone and the opening of a wider back-arc basin (model *1c113-70*; Fig. 7e).

397   The driving forces of plate tectonics across subduction-collision environment have been

398 largely discussed in term of crustal and mantle contributions [e.g. *Royden*, 1996; *Jolivet et al.*,

399 2009; *Faccenna and Becker*, 2010]. Recently, *Sternai et al.* [2014] proposed that extrusion

400 tectonics may be jointly driven by continental collision, slab roll-back and associated mantle

401 flow, the latter being particularly effective across hot and thin lithospheres. Indeed, the

402 viscosity contrast between such lithosphere and the underlying asthenosphere is low (i.e. ~10

403 Pa s; see Fig. 4 of *Sternai et al.* [2014]) promoting lithosphere/asthenosphere coupling. Our

404 results further suggest that the decrease of the bulk lithospheric strength by the magmatic

405 input results in a lower viscosity contrast along the lithosphere-asthenosphere boundary (i.e.

406 less than 10^2 Pa s; inset of Fig. 7e) therefore favoring the lithosphere/asthenosphere coupling.

407 This is a crucial mechanism for transmission of the velocities from the flowing mantle to the

408 crust (inset of Fig. 7e). In addition, sub-parallel crustal and asthenospheric velocity fields in

409 the back-arc domain where the upper lithosphere is thin, hot and therefore weak (Figs. 7d and

410 f), suggest that the strain is, at least to some extent, controlled by the underlying

411 asthenospheric flow in agreement with field observations [*Jolivet et al.*, 2009].

412   These results emphasize the role of mantle and crustal magmas on upper plate deformation

413 and lithosphere/asthenosphere coupling in subduction zone by decreasing the bulk

414 lithospheric strength. Applied to the strong downgoing lithosphere, such a melt-induced

415 lithospheric weakening could be considered as an efficient and required mechanism for slab

416 bending. Absence of slab partial melting in our experiments does not confirm this hypothesis

417 but fluid-induced weakening [*Gerya and Meilick*, 2011] related to slab hydration could be an

418 alternative explanation to reduce the slab strength. Normal faulting occurring in the upper,

419   brittle part of the slab would then have promoted this weakening effect by enhancing deep

420   slab hydration [*Faccenda et al.*, 2009].

421

422   *5.4.*   *Implications for the eastern Mediterranean region*

423   The late Cenozoic geodynamics of the eastern Mediterranean region, in particular coeval

424   retreat of the Hellenic subduction zone and collision across the Arabia-Eurasia margin

425   (Fig. 1c) [*Jolivet and Faccenna*, 2000], are consistently reproduced by our numerical

426   experiments (Figs. 4, 5 and S1). At depth, slab tearing occurs in these models along the

427   ocean-continent transition, which is consistent with seismic tomographic models proposing

428   the existence of two slab tears beneath western and eastern Anatolia (Fig. 2b) [*de Boorder et*

429   *al.*, 1998; *Wortel and Spakman*, 2000; *Li et al.*, 2008]. In addition, the toroidal asthenospheric

430   flow associated with slab roll-back and tearing in our experiments (Fig. 7) is consistent with

431   instantaneous 3D velocity field calculations for the flowing mantle [*Faccenna and Becker*,

432   2010] and other self-consistent 3D numerical studies applied to the eastern Mediterranean

433   region [*Li et al.*, 2013; *Capitanio*, 2014; *Duretz et al.*, 2014; *Sternai et al.*, 2014]. No clear

434   correlation, however, can be done between this toroidal flow and the *SKS* fast splitting

435   directions (Fig. 2b) [*Paul et al.*, 2014] suggesting a more complex relationship between the

436   SKS orientations and the asthenospheric flow pattern in this region (see discussion of *Le*

437   *Pichon and Kreemer* [2010]).

438   According to our results, slab tearing is correlated with the extrusion of crustal block from

439   the collisional domain toward the retreating subduction zone resulting in an overall

440   counterclockwise crustal velocity pattern (Figs. 7c and e), similar to the present-day crustal

441   kinematics across the study region deduced from GPS measurements (Fig. 2a) [*Reilinger et*

442   *al.*, 2006; *Le Pichon and Kreemer*, 2010]. The magnitude of these crustal velocities is also

443   consistent, with trench motion evolving from -2 cm yr^{-1} (advancing trench) to 3-7 cm yr^{-1}

444 (retreating trench) in models *2c89-60* and *1c113-70* and from 0.5 to 3 cm yr^{-1} for the Hellenic

445 trench (Fig. 6) [*Menant et al.*, 2016]. Acceleration of trench retreat, combined with an

446 advancing collisional front in our experiments as well as in the natural case can be related to

447 slab tears, which would confirm the middle-late Miocene age for slab tearing in the eastern

448 Mediterranean region [*Faccenna et al.*, 2006; *Dilek and Altunkaynak*, 2009; *Jolivet et al.*,

449 2015]. Small differences in these velocities may be, to some extent, due to the imposed free

450 slip conditions at the front and back boundaries ($z = 0$ and $z = 656$ km) laterally constraining

451 the crustal and mantle flow. Additional numerical experiments accounting for open

452 boundaries as well as the neighboring plates would then allow for more realistic boundary

453 conditions and therefore more accurate crustal velocities [*Yamato et al.*, 2009].

454   Mimicking the NAF accommodating the lateral extrusion of Anatolia since ~12 Ma,

455 localized strike-slip fault zone is fairly well reproduced in models characterized by a weak

456 overriding lithosphere (model *1c113-70*; Fig. 7e). Conversely, the propagation of this

457 localized strike-slip deformation is reduced within a strong lithosphere (model *2c89-60*; Fig.

458 7c). A weak overriding lithosphere also allows for opening of a wide back-arc basin (model

459 *1c113-70*; Fig. 7e) characterized by a ~50 km thick lithosphere (inset of Fig. 7e), which is

460 consistent with the present-day 40-50 km thick Aegean lithosphere [*Endrun et al.*, 2008]. In

461 addition, the exhumation in the back-arc domain of partially molten rocks as dome-like

462 structures (model *1c113*-70, Fig. 8c) mimic high-temperature MCCs with migmatitic core,

463 recognized in the Rhodope and Menderes massifs as well as in the Cyclades archipelago

464 [*Lister et al.*, 1984; *Bozkurt and Oberhänsli*, 2001; *Vanderhaeghe*, 2004; *Brun and Sokoutis*,

465 2007; *Jolivet et al.*, 2013]. These similarities suggest that the late Cenozoic deformation

466 pattern in the eastern Mediterranean region is controlled by the melt-induced weakening of

467 the lithosphere, especially in the Aegean back-arc domain where the emplacement of

468   magmatic bodies with a major crustal source component confirms an intense partial melting

469   of the lower crust [*Pe-Piper and Piper*, 2006; *Ersoy and Palmer*, 2013].

470   Space and time distribution of these magmatic products is also characterized by a first-

471   order southward migration driven by slab roll-back (see orange arrow, Fig. 1a) [*Pe-Piper and*

472   *Piper*, 2006; *Dilek and Altunkaynak*, 2009; *Ersoy and Palmer*, 2013], which is fairly well

473   reproduced in our models (Figs. 8 and 9). During the Miocene, this magmatic trend is

474   modulated by a second-order southwestward migration from the Menderes massif to the

475   Cyclades (see yellow arrow, Fig. 1a), which is also faithfully reproduced in our model with an

476   along-trench migration of partially molten rocks at the base of the crust controlled by the

477   toroidal asthenospheric flow related to slab tearing (Figs. 10c and d). This along-trench

478   migration of magmatic activity in the Aegean domain is accompanied by an increase of the

479   mantle-sourced magmas [*Jolivet et al.*, 2015], a feature that some experiments fail to

480   reproduce (model *1c113-70*; Fig. 9i), probably due to the insufficient numerical resolution

481   that buffered the mantle signature in the intensively partially molten continental crust.

482   Conversely, this trend is recognized in model *2c89-60* considering two-layer continental crust

483   (Fig. 8e), where increasing mantle-sourced magmatic component at the base of the overriding

484   crust mimics observations from the Miocene intrusions across the Cyclades [*Jolivet et al.*,

485   2015].

486   Eastern Anatolia is further characterized by a wide calc-alkaline to alkaline volcanic

487   province of late Miocene to Quaternary age (Fig. 1c) [*Keskin*, 2003]. In our experiments,

488   partially molten mantle and crust accumulate at the base of the collision zone due to the sub-

489   collisional slab detachment potentially resulting in such a wide magmatic activity (Figs. 8e

490   and 9e). Later alkaline volcanism emplaced in the eastern Mediterranean region resulting

491   from the adiabatic partial melting of depleted asthenosphere [*Keskin*, 2003; *Ersoy and*

Palmer, 2013] which can be related to the asthenospheric upwelling associated with slab

tearing and intense lithospheric stretching reproduced in our experiments (Figs. 8i and 9i).

Our results clearly emphasize the role of slab roll-back and tearing and related

asthenospheric flow on the late Cenozoic magmatic and tectonic evolution of the eastern

Mediterranean region. Of course, these 3D models cannot fully assess the natural complexity

of the eastern Mediterranean subduction zone, characterized by successive oceanic and

continental subduction events and, possibly, several slab tearing processes [*Stampfli and*

Borel, 2002; *Menant et al.*, 2016]. However, consistency between our experiments and the

natural case in terms of crustal kinematics, deformation and magmatic evolution suggests that

we reproduce the first-order crustal and mantle dynamics of the eastern Mediterranean

subduction zone during the late Cenozoic.

6.   Conclusions

Using a 3D high-resolution coupled petrological and thermo-mechanical model integrating

experimentally calibrated non-Newtonian crustal and mantle rheologies, we are able to

reproduce the first-order geodynamic evolution of a coeval oceanic and continental

subduction zone characterized by slab roll-back and tearing. Integrating slab dehydration,

fluid transport and partial melting processes, our experiments demonstrated (1) the control of

3D subduction dynamics and related asthenospheric flow on space and time evolution of

magmas from the upper mantle to the overriding crust and (2) the significant role of melt-

induced rheological weakening on lithospheric deformation. In detail, we reach the following

conclusions.

- Slab dynamics and associated mantle flow affect magma genesis and transport within the

hydrated mantle wedge. A typical asthenospheric return flow in the mantle wedge tends to

delay the ascent of partially molten rocks. Conversely, asthenospheric upwelling associated

with slab roll-back and tearing allows for a fast ascent of the magmatic sources as plumes with variable morphologies. A slow sinking slab thus promotes the development of along-trench Rayleigh-Taylor instabilities at the slab-mantle interface favoring finger-like plumes, while fast evolving subduction zone and associated asthenospheric flow facilitate the ascent of large amount of partially molten material as wave-like plumes.

- During their emplacement, both mantle- and crust-derived magmas contribute to the reduction of the bulk strength of the overriding lithosphere thereby affecting the deformation pattern. The ascent of large amounts of partially molten material within the stretched crust localizes deformation along dome-like structures. The crustal deformation is then characterized by strike-slip faulting and stretching that accommodate the lateral extrusion of crustal block and slab roll-back, respectively. This melt-induced weakening of the crust also promotes the lithosphere/asthenosphere coupling and the transmission of the velocities from the flowing asthenosphere to the crust, supporting the hypothesis that the mantle flow may drag the crust thereby affecting surface deformation.

- The kinematic, strain and magmatic evolution of the eastern Mediterranean region deduced from geological and geophysical constraints are reasonably well reproduced by our experiments suggesting a major control of subduction dynamics and related asthenospheric flow on the magmatic evolution. As such, we propose that roll-back and tearing of the eastern Mediterranean slab may have controlled, respectively, the southward and southwestward migration of magmatic centers since the late Cenozoic.

References

Arculus, R. J. (1994), Aspects of magma genesis in arcs, *Lithos*, *33*(1-3), 189–208, doi:10.1016/0024-4937(94)90060-4.

Bouilhol, P., V. Magni, J. van Hunen, and L. Kaislaniemi (2015), A numerical approach to melting in warm subduction zones, *Earth Planet. Sci. Lett.*, *411*, 37–44, doi:10.1016/j.epsl.2014.11.043.

Bozkurt, E., and R. Oberhänsli (2001), Menderes Massif (Western Turkey): structural, metamorphic and magmatic evolution - a synthesis, *Int. J. Earth Sci.*, *89*(4), 679–708, doi:10.1007/s005310000173.

Brun, J.-P., and D. Sokoutis (2007), Kinematics of the Southern Rhodope Core Complex (North Greece), *Int. J. Earth Sci.*, *96*(6), 1079–1099, doi:10.1007/s00531-007-0174-2.

Capitanio, F. A. (2014), The dynamics of extrusion tectonics: Insights from numerical modeling, *Tectonics*, *33*(12), 2361–2381, doi:10.1002/2014TC003688.

de Boorder, H., W. Spakman, S. H. White, and M. J. R. Wortel (1998), Late Cenozoic mineralization, orogenic collapse and slab detachment in the European Alpine Belt, *Earth Planet. Sci. Lett.*, *164*(3-4), 569–575, doi:10.1016/S0012-821X(98)00247-7.

Dilek, Y., and S. Altunkaynak (2009), Geochemical and temporal evolution of Cenozoic magmatism in western Turkey: mantle response to collision, slab break-off, and lithospheric tearing in an orogenic belt, *Spec. Publ. - Geol. Soc. London*, *311*(1), 213–233, doi:10.1144/SP311.8.

Duretz, T., T. V. Gerya, and W. Spakman (2014), Slab detachment in laterally varying subduction zones: 3-D numerical modeling, *Geophys. Res. Lett.*, *41*(6), 1951–1956, doi:10.1002/2014GL059472.

Endrun, B., T. Meier, S. Lebedev, M. Bohnhoff, G. Stavrakakis, and H.-P. Harjes (2008), *S* velocity structure and radial anisotropy in the Aegean region from surface wave dispersion, *Geophys. J. Int.*, *174*, 593-616, doi:10.1111/j.1365-246X.2008.03802.x.

Ersoy, E. Y., and M. R. Palmer (2013), Eocene-Quaternary magmatic activity in the Aegean: Implications for mantle metasomatism and magma genesis in an evolving orogeny, *Lithos*, doi:10.1016/j.lithos.2013.06.007.

Faccenda, M., T. V. Gerya, and L. Burlini (2009), Deep slab hydration induced by bending-related variations in tectonic pressure, *Nat. Geosci.*, *2*(11), 790–793, doi:10.1038/ngeo656.

Faccenna, C., O. Bellier, J. Martinod, C. Piromallo, and V. Regard (2006), Slab detachment beneath eastern Anatolia: A possible cause for the formation of the North Anatolian fault, *Earth Planet. Sci. Lett.*, *242*(1-2), 85–97, doi:10.1016/j.epsl.2005.11.046.

Faccenna, C., and T. W. Becker (2010), Shaping mobile belts by small-scale convection, *Nature*, *465*(7298), 602–605, doi:10.1038/nature09064.

578   Gerya, T. V., and D. A. Yuen (2007), Robust characteristics method for modelling multiphase visco-
579   elasto-plastic thermo-mechanical problems, *Phys. Earth Planet. Inter.*, *163*(1-4), 83–105,
580   doi:10.1016/j.pepi.2007.04.015.

581   Gerya, T. V., and F. I. Meilick (2011), Geodynamic regimes of subduction under an active margin:
582   effects of rheological weakening by fluids and melts, *J. Metamorph. Geol.*, *29*(1), 7–31,
583   doi:10.1111/j.1525-1314.2010.00904.x.

584   Hawkesworth, C. J. (1997), U-Th Isotopes in Arc Magmas: Implications for Element Transfer from
585   the Subducted Crust, *Science*, *276*(5312), 551–555, doi:10.1126/science.276.5312.551.

586   Hildreth, W., and S. Moorbath (1988), Crustal contributions to arc magmatism in the Andes of Central
587   Chile, *Contrib. Mineral. Petrol.*, *98*(4), 455–489, doi:10.1007/BF00372365.

588   Huw Davies, J., and F. von Blanckenburg (1995), Slab breakoff: A model of lithosphere detachment
589   and its test in the magmatism and deformation of collisional orogens, *Earth Planet. Sci. Lett.*,
590   *129*(1-4), 85–102, doi:10.1016/0012-821X(94)00237-S.

591   Jadamec, M. A., and M. I. Billen (2010), Reconciling surface plate motions with rapid three-
592   dimensional mantle flow around a slab edge, *Nature*, *465*(7296), 338–341,
593   doi:10.1038/nature09053.

594   Johnson, H. P., and M. J. Pruis (2003), Fluxes of fluid and heat from the oceanic crustal reservoir,
595   *Earth Planet. Sci. Lett.*, *216*(4), 565–574, doi:10.1016/S0012-821X(03)00545-4.

596   Jolivet, L., and C. Faccenna (2000), Mediterranean extension and the Africa-Eurasia collision,
597   *Tectonics*, *19*(6), 1095–1106, doi:10.1029/2000TC900018.

598   Jolivet, L., C. Faccenna, and C. Piromallo (2009), From mantle to crust: Stretching the Mediterranean,
599   *Earth Planet. Sci. Lett.*, *285*(1-2), 198–209, doi:10.1016/j.epsl.2009.06.017.

600   Jolivet, L. et al. (2013), Aegean tectonics: Strain localisation, slab tearing and trench retreat,
601   *Tectonophysics*, *597-598*, 1–33, doi:10.1016/j.tecto.2012.06.011.

602   Jolivet, L. et al. (2015), The geological signature of a slab tear below the Aegean, *Tectonophysics*,
603   *659*, 166–182, doi:10.1016/j.tecto.2015.08.004.

604   Katz, R. F., M. Spiegelman, and C. H. Langmuir (2003), A new parameterization of hydrous mantle
605   melting, *Geochem. Geophys. Geosyst.*, *4*(9), n/a–n/a, doi:10.1029/2002GC000433.

606   Keskin, M. (2003), Magma generation by slab steepening and breakoff beneath a subduction-accretion
607   complex: An alternative model for collision-related volcanism in Eastern Anatolia, Turkey,
608   *Geophys. Res. Lett.*, *30*(24), doi:10.1029/2003GL018019.

609   Le Pichon, X., and C. Kreemer (2010), The Miocene-to-Present Kinematic Evolution of the Eastern
610   Mediterranean and Middle East and Its Implications for Dynamics, *Annu. Rev. Planet. Sci.* *38*(1),
611   323-351, doi:10.1146/annurev-earth-040809-152419.

612 Li, C., R. D. van der Hilst, E. R. Engdahl, and S. Burdick (2008), A new global model for P wave
613   speed variations in Earth's mantle, *Geochem. Geophys. Geosyst.*, *9*(5),
614   doi:10.1029/2007GC001806.

615 Li, Z.-H., Z. Xu, T. Gerya, and J.-P. Burg (2013), Collision of continental corner from 3-D numerical
616   modeling, *Earth Planet. Sci. Lett.*, *380*, 98–111, doi:10.1016/j.epsl.2013.08.034.

617 Lister, G. S., G. Banga, and A. Feenstra (1984), Metamorphic core complexes of Cordilleran type in
618   the Cyclades, Aegean Sea, Greece, *Geology*, *12*(4), 221, doi:10.1130/0091-
619   7613(1984)12<221:MCCOCT>2.0.CO;2.

620 Magni, V., C. Faccenna, J. van Hunen, and F. Funiciello (2014), How collision triggers backarc
621   extension: Insight into Mediterranean style of extension from 3-D numerical models, *Geology*,
622   *42*(6), 511–514, doi:10.1130/G35446.1.

623 Menant, A., L. Jolivet, and B. Vrielynck (2016), From crustal to mantle dynamics, insight from
624   kinematic reconstructions and magmatic evolution of the eastern Mediterranean region since the
625   late Cretaceous, *Tectonophysics*.

626 Nikolaeva, K., T. V. Gerya, and J. A. D. Connolly (2008), Numerical modelling of crustal growth in
627   intraoceanic volcanic arcs, *Phys. Earth Planet. Inter.*, *171*(1-4), 336–356,
628   doi:10.1016/j.pepi.2008.06.026.

629 Paul, A., H. Karabulut, A. K. Mutlu, and G. Salaün (2014), A comprehensive and densely sampled
630   map of shear-wave azimuthal anisotropy in the Aegean–Anatolia region, *Earth Planet. Sci. Lett.*,
631   *389*, 14–22, doi:10.1016/j.epsl.2013.12.019.

632 Pe-Piper, G., and D. J. W. Piper (2006), Unique features of the Cenozoic igneous rocks of Greece,
633   *Spec. Pap. - Geol. Soc. Am.*, *409*, 259–282.

634 Ranalli, G. (1995), *Rheology of the Earth*, Chapman & Hall., London, UK.

635 Reilinger, R. et al. (2006), GPS constraints on continental deformation in the Africa-Arabia-Eurasia
636   continental collision zone and implications for the dynamics of plate interactions, *J. Geophys.*
637   *Res.*, *111*(B5), doi:10.1029/2005JB004051.

638 Royden, L. (1996), Coupling and decoupling of crust and mantle in convergent orogens: Implications
639   for strain partitioning in the crust, *J. Geophys. Res.*, *101*(B8), 17679, doi:10.1029/96JB00951.

640 Schmeling, H. et al. (2008), A benchmark comparison of spontaneous subduction models—Towards a
641   free surface, *Phys. Earth Planet. Inter.*, *171*(1-4), 198–223, doi:10.1016/j.pepi.2008.06.028.

642 Şengör, A. M. C., O. Tüysüz, C. İmren, M. Sakınç, H. Eyidoğan, N. Görür, X. Le Pichon, and C.
643   Rangin (2005), The North Anatolian Fault: A New Look, *Annu. Rev. Earth Planet. Sci.*, *33*(1),
644   37–112, doi:10.1146/annurev.earth.32.101802.120415.

645 Stampfli, G. M., and G. D. Borel (2002), A plate tectonic model for the Paleozoic and Mesozoic
646   constrained by dynamic plate boundaries and restored synthetic oceanic isochrons, *Earth Planet.*
647   *Sci. Lett.*, *196*(1-2), 17–33, doi:10.1016/S0012-821X(01)00588-X.

648 Sternai, P., L. Jolivet, A. Menant, and T. Gerya (2014), Driving the upper plate surface deformation by
649   slab rollback and mantle flow, *Earth Planet. Sci. Lett.*, *405*, 110–118,
650   doi:10.1016/j.epsl.2014.08.023.

651 Turcotte, D. L., and G. Schubert (2002), *Geodynamics*, Cambridge University Press., Cambridge, UK.

652 Vanderhaeghe, O. (2004), Structural development of the Naxos migmatite dome, *Spec. Pap. - Geol.*
653   *Soc. Am.*, *380*, 211–227.

654 Watts, A. B., and E. B. Burov (2003), Lithospheric strength and its relationship to the elastic and
655   seismogenic layer thickness, *Earth Planet. Sci. Lett.*, *213*, 113-131, doi:10.1016/S0012-
656   821X(03)00289-9.

657 Wortel, M. J. R., and W. Spakman (2000), Subduction and Slab Detachment in the Mediterranean-
658   Carpathian Region, *Science*, *290*(5498), 1910–1917, doi:10.1126/science.290.5498.1910.

659 Yamato, P., L. Husson, J. Braun, C. Loiselet, and C. Thieulot (2009), Influence of surrounding plates
660   on 3D subduction dynamics, *Geophysical Research Letters*, *36*(L07303),
661   doi:10.1029/2008GL036942.

662 Zhu, G., T. V. Gerya, D. A. Yuen, S. Honda, T. Yoshida, and J. A. D. Connolly (2009), Three-
663   dimensional dynamics of hydrous thermal-chemical plumes in oceanic subduction zones,
664   *Geochem. Geophys. Geosyst.*, *10*(11), doi:10.1029/2009GC002625.

665 Zhu, G., T. V. Gerya, P. J. Tackley, and E. Kissling (2013), Four-dimensional numerical modeling of
666   crustal growth at active continental margins, *Journal of Geophysical Research: Solid Earth*,
667   *118*(9), 4682–4698, doi:10.1002/jgrb.50357.

668
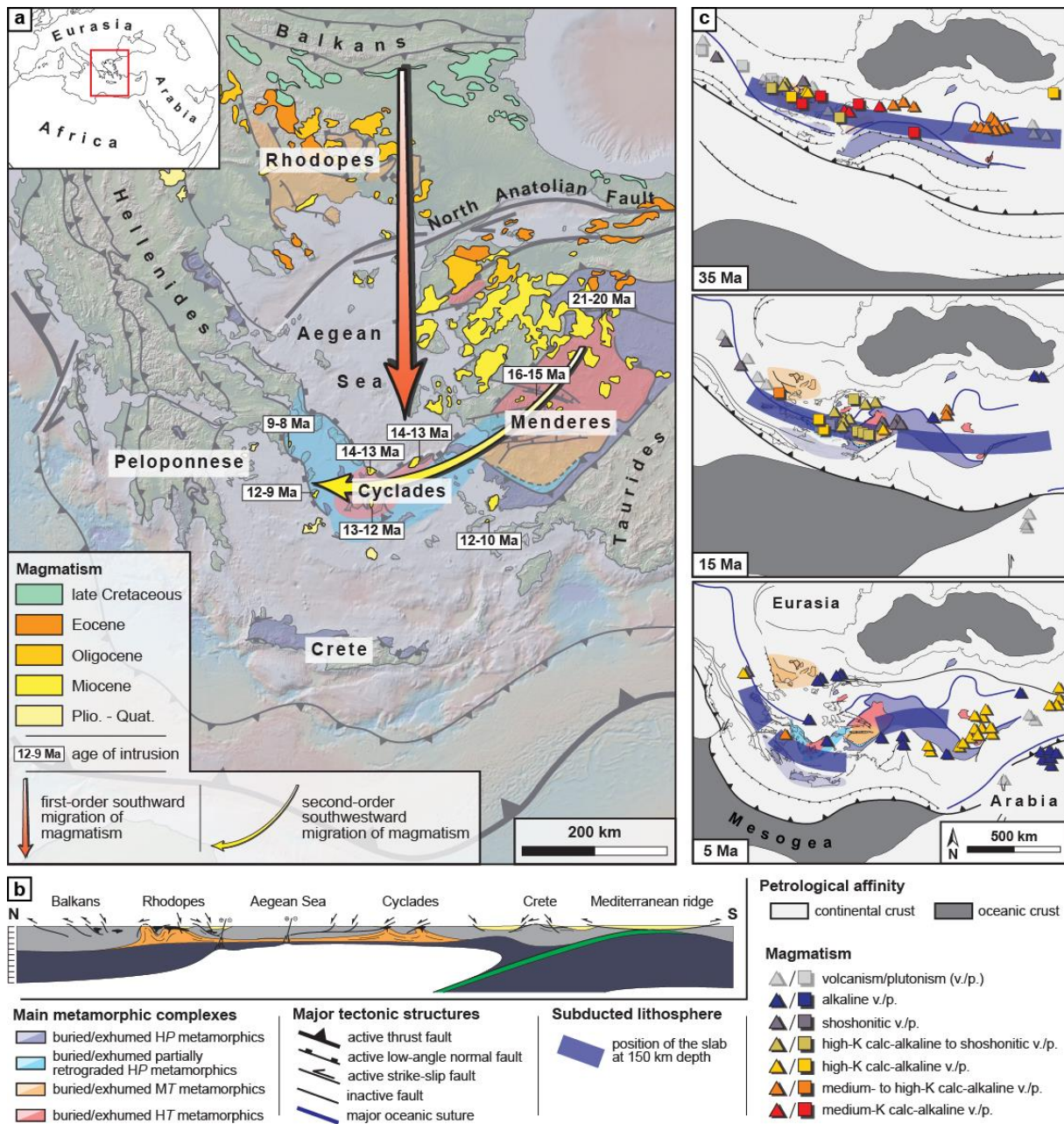
Fig. 1: Late Cenozoic geodynamic evolution of the eastern Mediterranean region. (a) Tectonic map of the eastern Mediterranean region showing the spatial distribution of the magmatism since the late Cretaceous. Red and yellow arrows show, respectively, the first-order southward migration of the magmatism since the late Cretaceous and the second-order southwestward migration of the magmatism during the Miocene. (b) Present-day N-S cross-section across the Rhodope-Aegean region. (c) Paleotectonic maps of the eastern Mediterranean region at 35, 15 and 5 Ma showing the spatial distribution of contemporaneous magmatic occurrences. Modified from *Menant et al.* [2016].
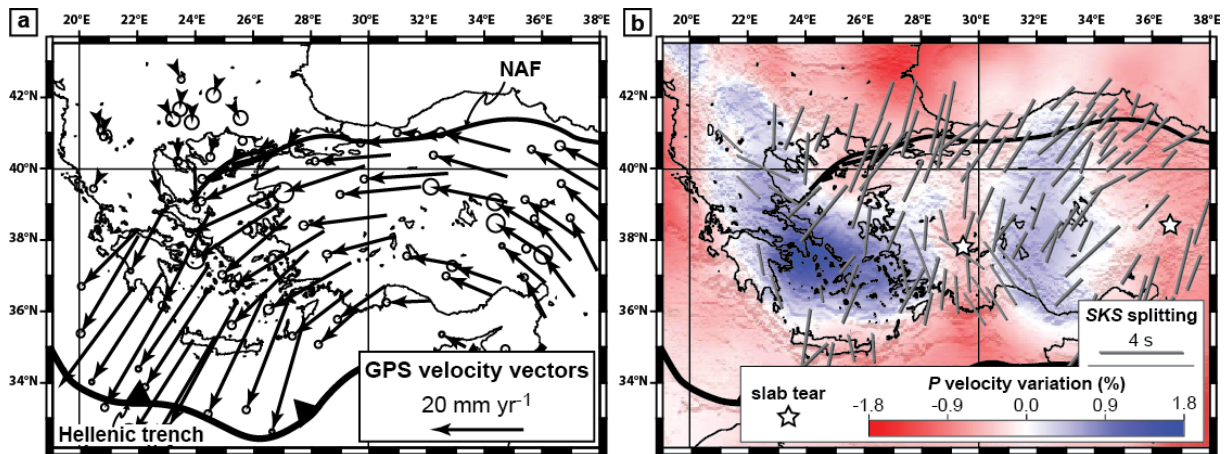
Fig. 2: Geophysical maps of the eastern Mediterranean region. (a) GPS velocities relative to stable Eurasia with 1σ confidence ellipses [*Reilinger et al.*, 2006]. (b) Seismic tomographic model showing the *Vp* anomalies at ~150 km depth [*Li et al.*, 2008]. Slab tears suspected in the region are highlighted by white stars. Station-averaged SKS splitting data are also highlighted [*Paul et al.*, 2014].
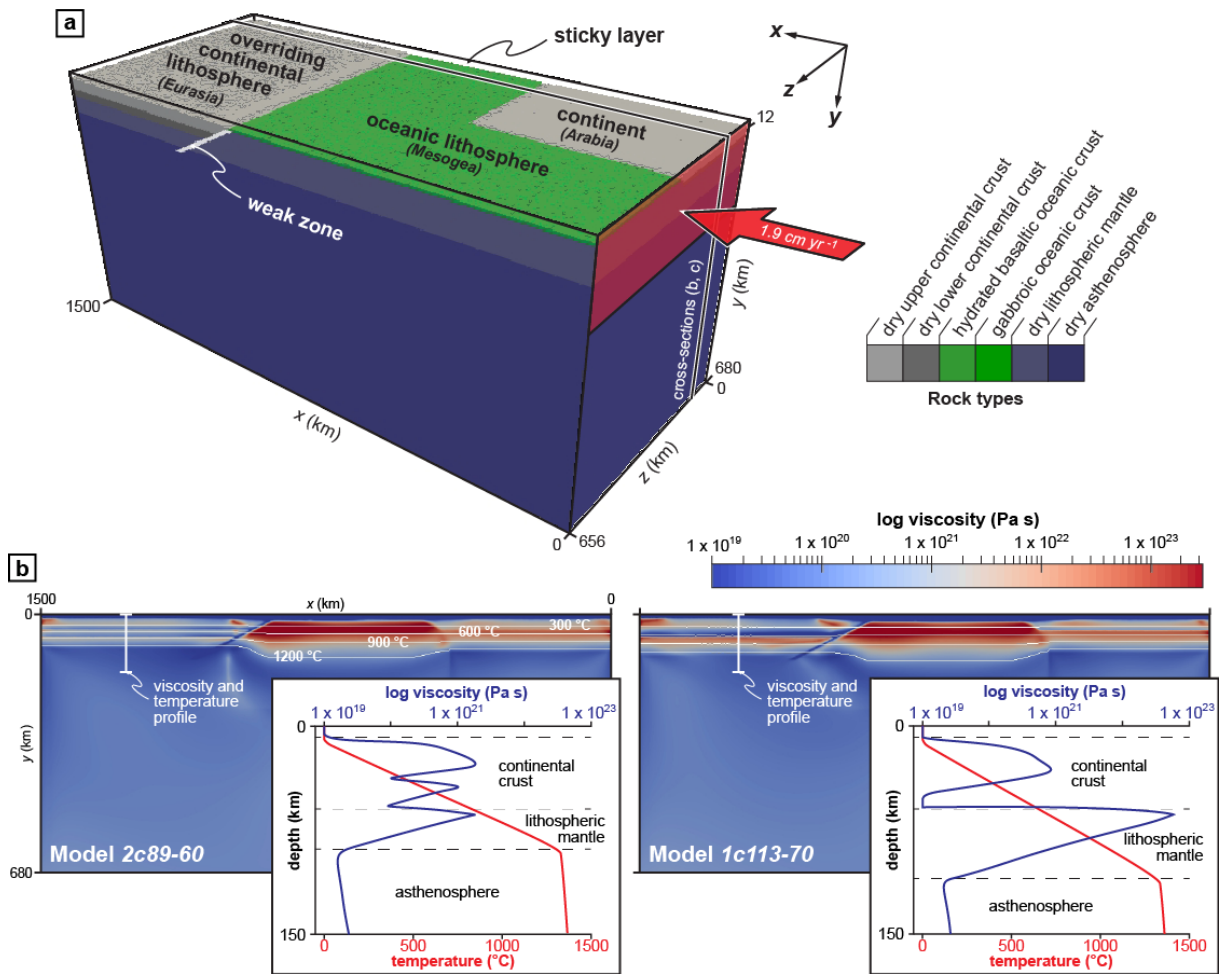
Fig. 3: Initial model setup. (a) 3D model domain with colors representing the different rock types. Air and sea water phases (composing the sticky layer) are cut off for clarity. b) *x-y* viscosity cross-sections of the initial model domain with a two-layer (left panel) and one-layer (right panel) continental crust. White lines represent 300, 600, 900 and 1200 °C isotherms. Vertical viscosity (blue) and temperature (red) profiles are shown as inset for each model.
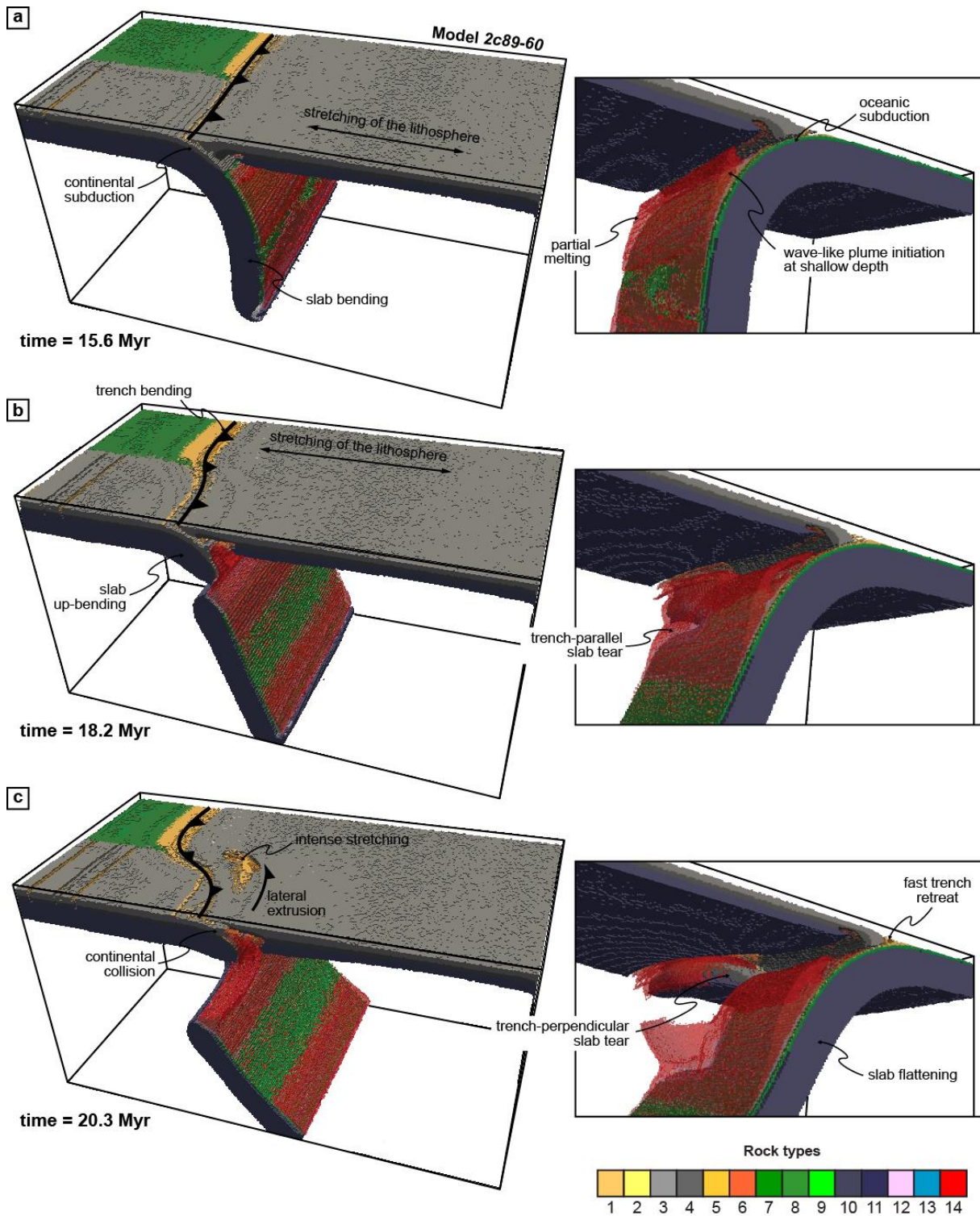
Fig. 4: Evolution of the reference model *2c93-60* (with a two-layer continental crust). (a, b, c) 3D lateral view of the subduction zone (left panels) and zoom on the mantle wedge (right panels) for selected time steps. Colors represent the different rock types: 1 – sediments; 2 – partially molten sediments; 3/4 – dry upper/lower continental crust; 5/6 – hydrated/partially molten continental crust; 7 – dry oceanic crust; 8/9 – hydrated/partially molten oceanic crust; 10 – dry lithospheric mantle; 11 – dry asthenosphere; 12/13 – hydrated/serpentinized mantle; 14 – partially molten mantle. Asthenosphere and other phases are cut off for clarity.
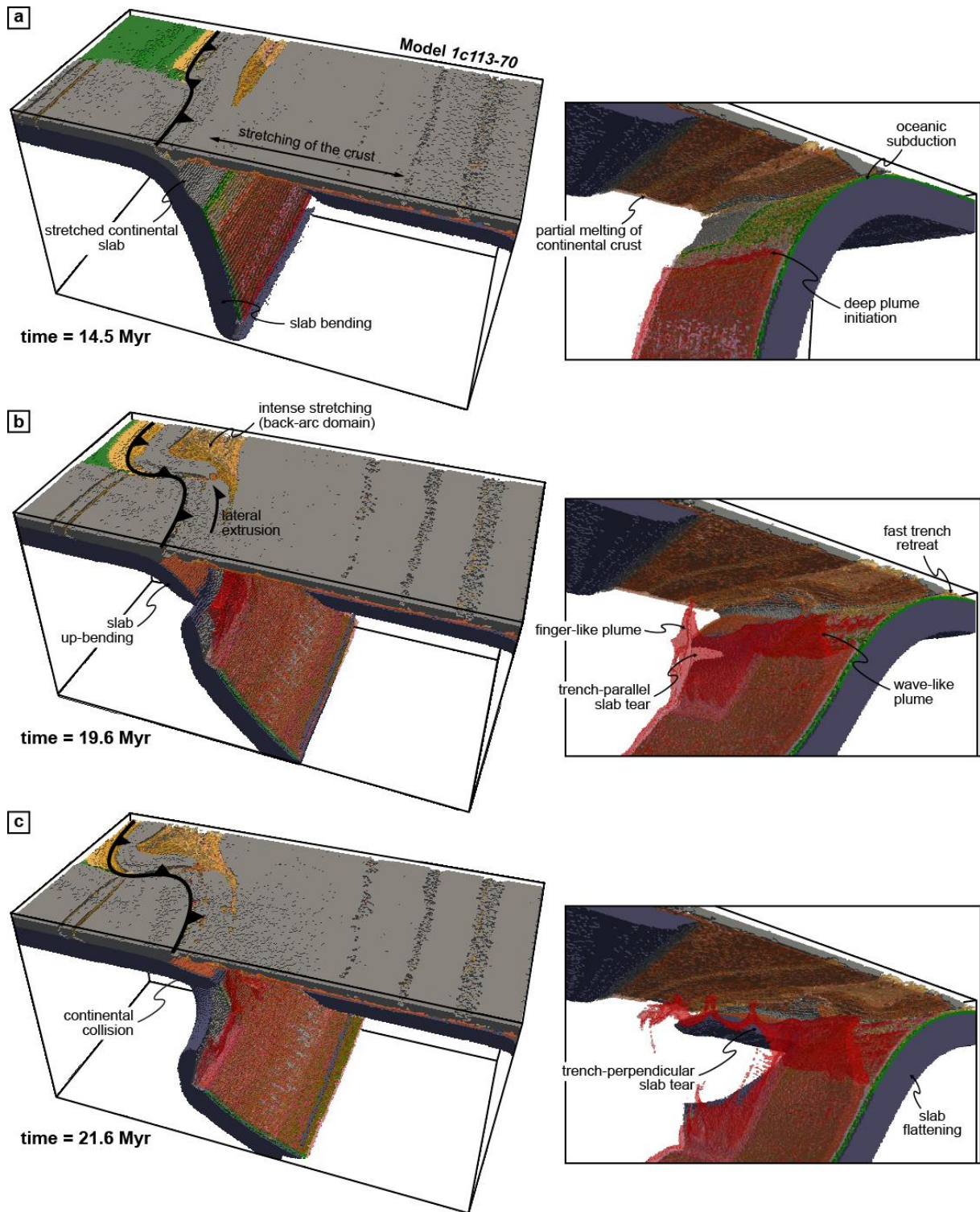
Fig. 5: Evolution of the model 1*c113-70* (with a one-layer continental crust). (a, b, c) 3D lateral view of the subduction zone (left panels) and zoom on the mantle wedge (right panels) for selected time steps. Colors represent the different rock types (see Fig. 4 for detailed legend). Asthenosphere and other phases are cut off for clarity.
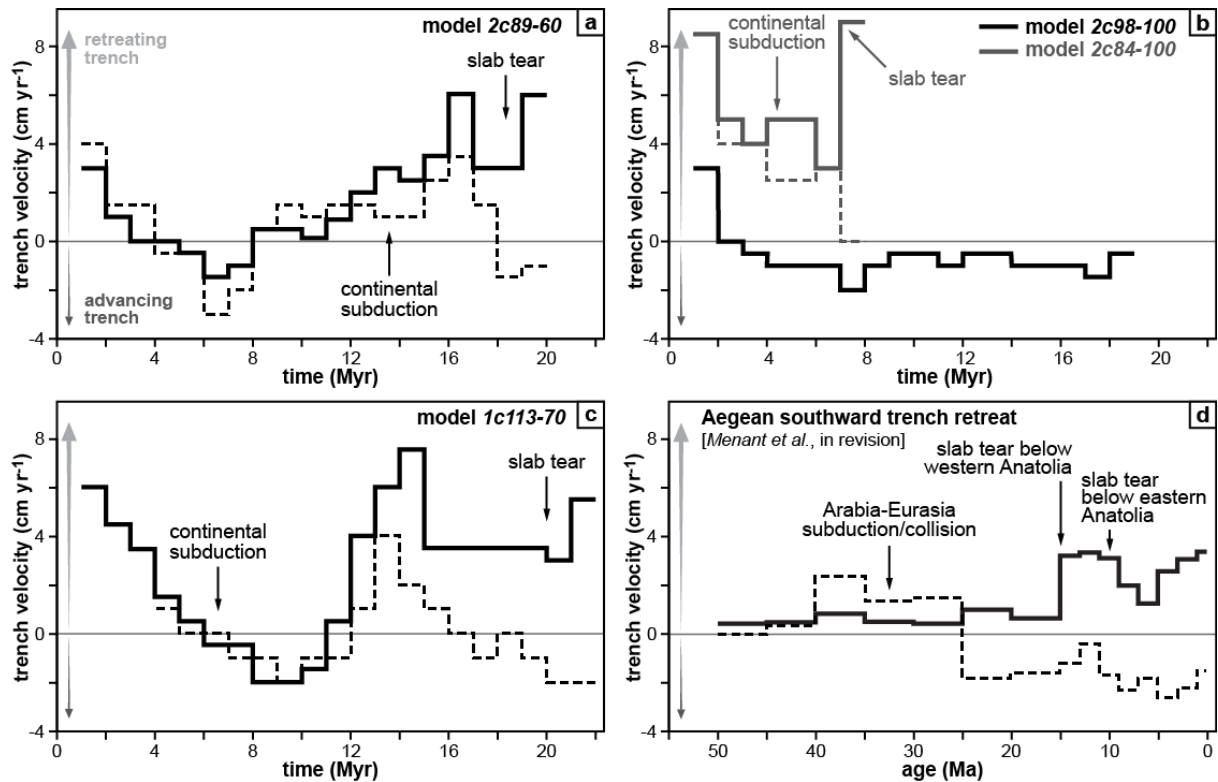
Fig. 6: Time-trench velocity diagram showing the trench migration of both oceanic and oceanic-continental subduction zones obtained from models *2c89-60* (a), *2c98-100*, *2c84-100* (b) and *1c113-70* (c) and from kinematic reconstructions of the eastern Mediterranean region (d) [*Menant et al.*, 2016]. Solid and dashed lines correspond to only oceanic (or Hellenic) and oceanic-continental (or eastern Anatolia) subduction zones, respectively. Positive and negative distances correspond to retreating and advancing trench, respectively. The initiation of continental subduction and slab tearing processes are highlighted for each diagram.
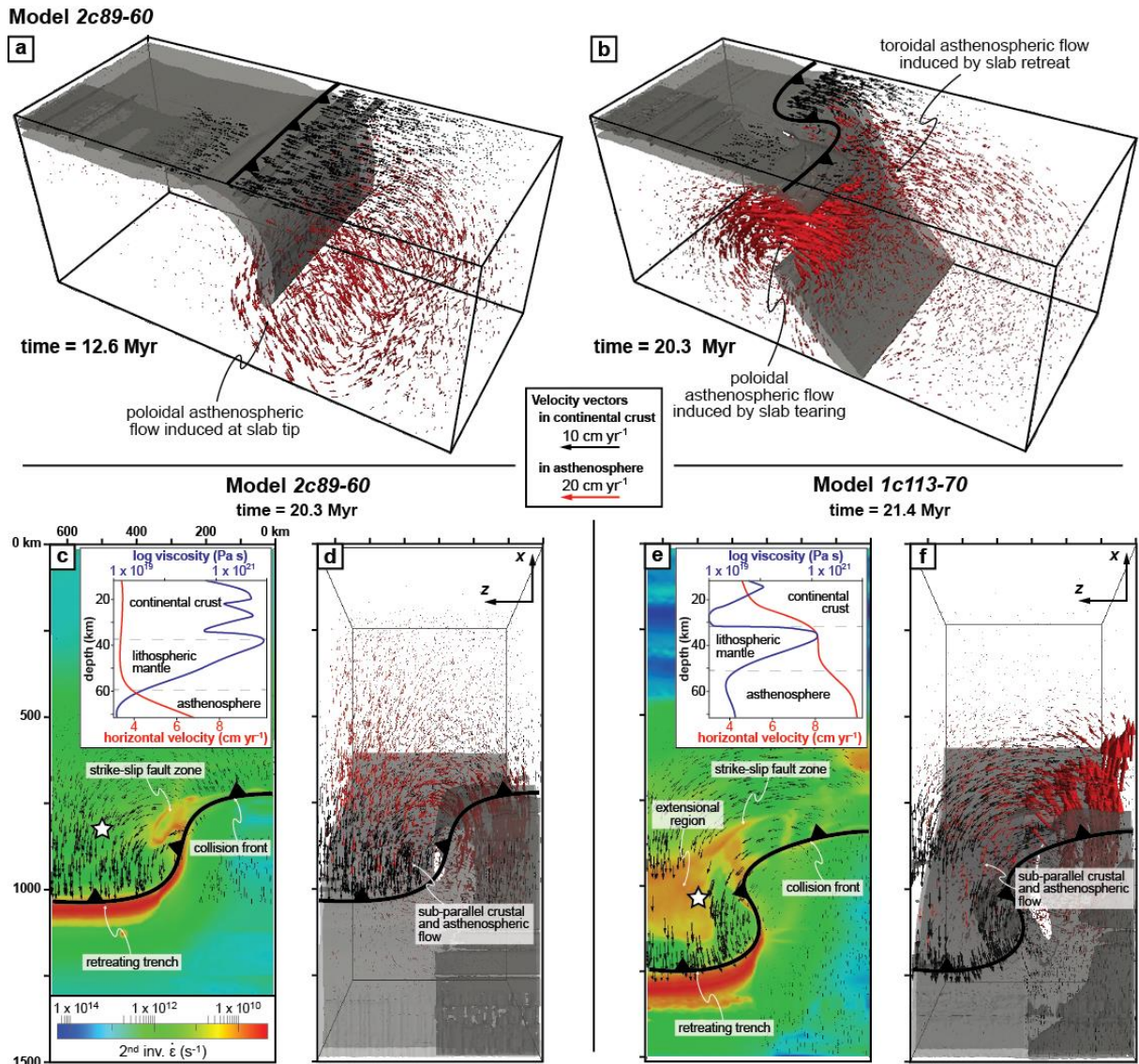
Fig. 7: Asthenospheric and crustal flow evolution and crustal strain rate in performed numerical experiments. (a, b) 3D view of the subduction zone of model *2c93*-60 at two selected time steps (i.e. before and after slab tearing) showing the slab geometry (iso-viscosity contour equal to 10^{23} Pa.s) and velocity vectors in the continental crust (black arrows) and asthenosphere (red arrows). (c, e) *x-z* plan view of selected time step showing the second invariant of the strain rate tensor in interacting lithospheres of models *2c93-60* and *1c113-70*. Vertical viscosity (blue) and velocity (red) profiles are shown as inset for each extensional domain (see the white star for the location of the vertical profile). (d, f) *x-z* plan view of selected time step showing the velocity vectors in the continental crust and asthenosphere. Scale of velocity vectors is twice larger in continental crust than in asthenosphere.
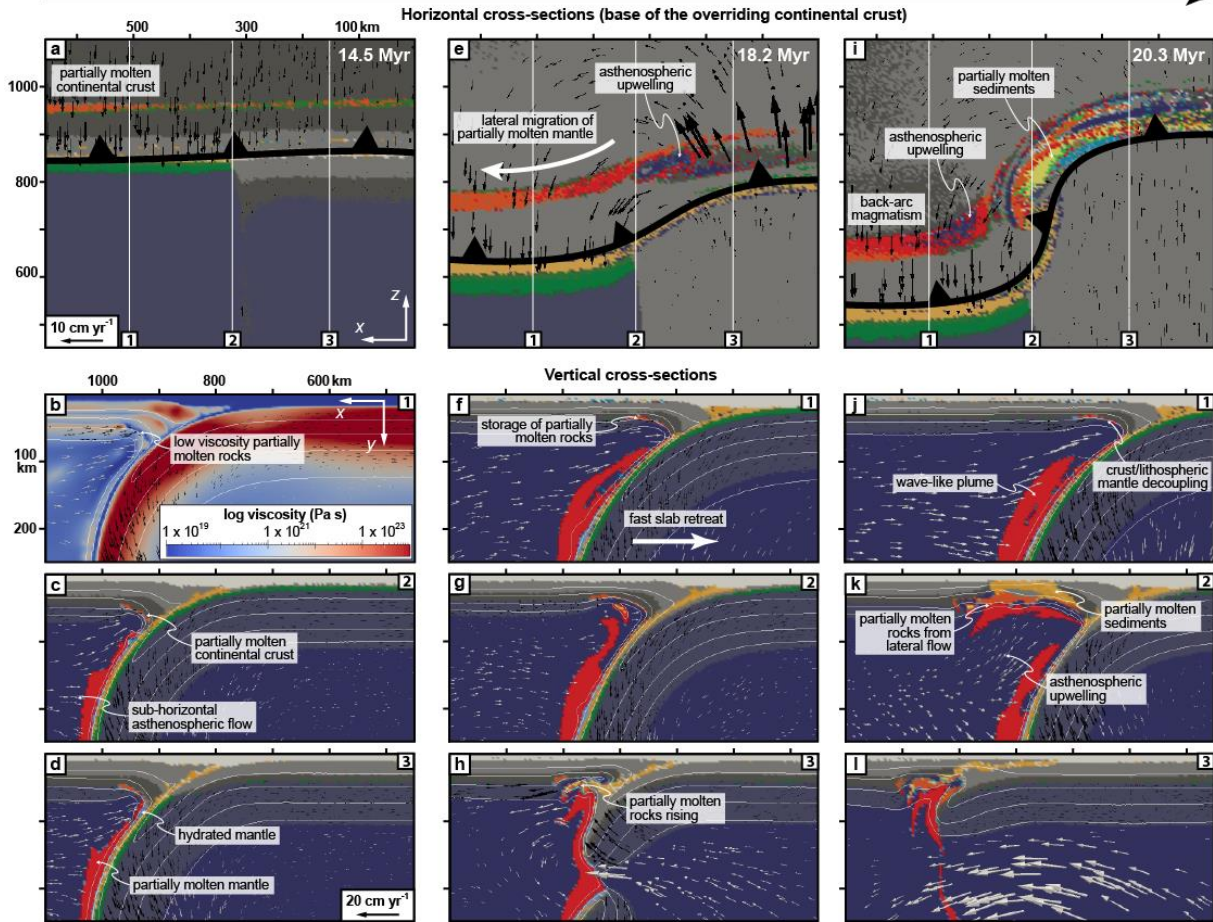
Fig. 8: Evolution of magmatism in reference model *2c93-60*. *x-z* plan views (a, e, i) and *x-y* cross-sections (b, c, d, f, g, h, j, k, l) of the subduction zone for selected time steps. Colors represent the different rock types (see Fig. 4 for detailed legend), except for cross-section (b) where the viscosity is mapped. Black and white arrows represent velocity vectors in the continental crust (top panels) or lithospheric mantle (bottom panels) and the asthenosphere, respectively. Scale of velocity vectors is twice larger in top panels than in bottom panels. White lines (bottom panels) represent 300, 600, 900 and 1200 °C isotherms.

**Fig. 9:** Evolution of magmatism in model *1c113-70*. *x-z* plan views (a, e, i) and *x-y* cross-sections (b, c, d, f, g, h, j, k, l) of the subduction zone for selected time steps. Colors represent the different rock types (see Fig. 4 for detailed legend), except for cross-section (b) where the viscosity is mapped. Black and white arrows represent velocity vectors in the continental crust (top panels) or lithospheric mantle (bottom panels) and the asthenosphere, respectively. Scale of velocity vectors is twice larger in top panels than in bottom panels. White lines (bottom panels) represent 300, 600, 900 and 1200 °C isotherms.
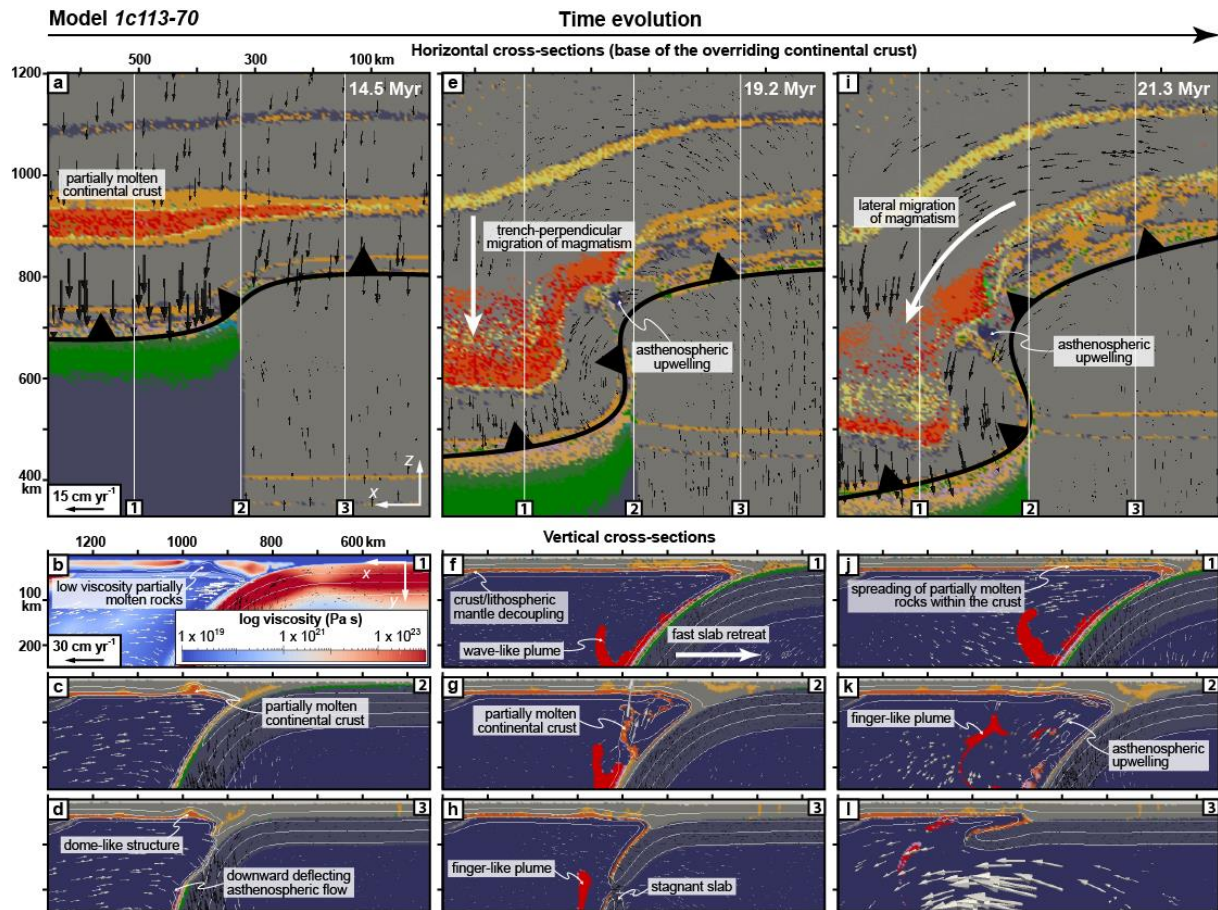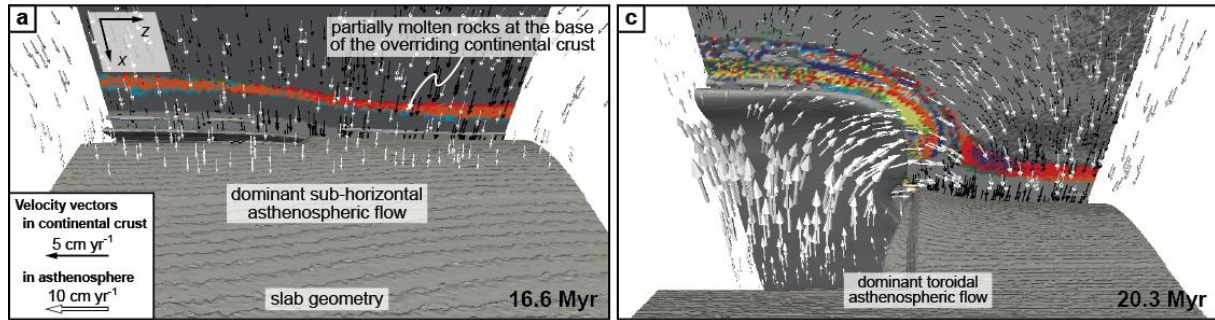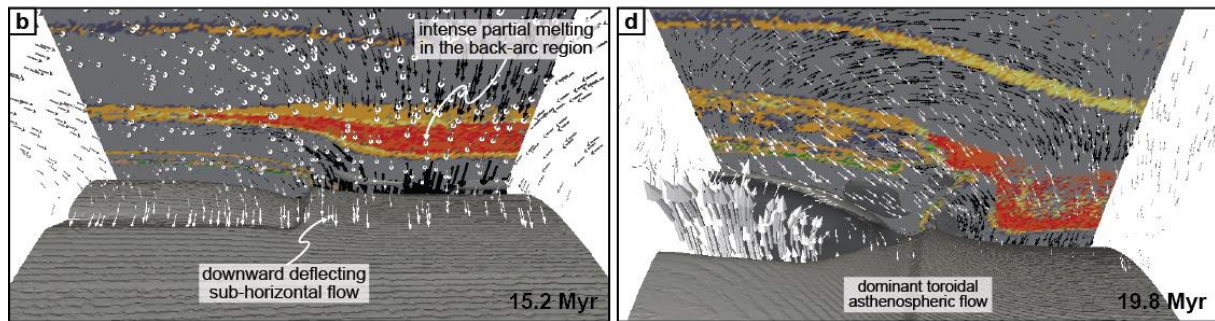
Fig. 10: View from below of the mantle wedge of selected models showing the relation between magmatic evolution at the base of the overriding crust and subduction-related asthenospheric flow for two selected time steps. (a, c) *x-z* plan view and slab geometry evolution of reference model *2c93-60*. (b, d) *x-z* plan view and slab geometry evolution of reference model *1c113-70*. On *x-z* plan view, colors represent the different rock types (see Fig. 4 for detailed legend). The slab geometry is visualized through an iso-viscosity contour equal to 10^{23} Pa.s. Black and white arrows represent velocity vectors in the continental crust and the asthenosphere, respectively. Scale of velocity vectors is twice larger in continental crust than in asthenosphere.

Supplementary material

746

747 **Numerical approach and governing equations**

748 *Conservation equations*

749   In our experiments, we model rocks as an incompressible fluid through the 3D mass

750 conservation equation:

751
$$\nabla \cdot \vec{u} = \frac{\partial v_x}{\partial x} + \frac{\partial v_y}{\partial y} + \frac{\partial v_z}{\partial z} = 0 \tag{1}$$

752   where v_x, v_y and v_z are the components of the velocity vector $\vec{u}$. The momentum of this

753 incompressible fluid thus occurs as a 3D creeping (or laminar) flow meaning that the viscous

754 forces are significantly higher than the inertial ones (i.e. Reynolds number << 1). This

755 momentum is then solved using Stokes equation:

756
$$\frac{\partial \sigma_{xx}}{\partial x} + \frac{\partial \sigma_{xy}}{\partial y} + \frac{\partial \sigma_{xz}}{\partial z} = \frac{\partial p}{\partial x}$$

757
$$\frac{\partial \sigma_{yx}}{\partial x} + \frac{\partial \sigma_{yy}}{\partial y} + \frac{\partial \sigma_{yz}}{\partial z} = \frac{\partial p}{\partial y} - g\,\rho \tag{2}$$

758
$$\frac{\partial \sigma_{zx}}{\partial x} + \frac{\partial \sigma_{zy}}{\partial y} + \frac{\partial \sigma_{zz}}{\partial z} = \frac{\partial p}{\partial z}$$

759   where σ_{ij} are the components of the deviatoric stress tensor, p is the pressure, g is the

760 gravitational acceleration and ρ is the density (Table S1). Finally, heat diffusion in our

761 experiments is solved using the Lagrangian heat conservation equation:

762
$$\rho\,C_P\,\frac{DT}{Dt} = -\frac{\partial q_x}{\partial x} - \frac{\partial q_y}{\partial y} - \frac{\partial q_z}{\partial z} + H_r + H_a + H_s \tag{3}$$

763   where C_p is the isobaric heat capacity, T is the temperature, t is the time, H_r is the

764   radiogenic heat production, H_a is the adiabatic heat production, H_s is the shear heating and q_x,

765   q_y and q_z are the components of the 3D heat flow solved as:

766      $$q_x = -k \frac{\partial T}{\partial x}$$

767      $$q_y = -k \frac{\partial T}{\partial y} \tag{4}$$

768      $$q_z = -k \frac{\partial T}{\partial z}$$

769   where k is the thermal conductivity depending on the temperature and rock composition

770   (Table S1). Heat advection is then solved based on marker technics [*Gerya and Yuen*, 2007].

771   Surface processes are implemented using a highly simplified gross-scale erosion-

772   sedimentation law (see details in *Gerya and Yuen* [2007]). Considering these physical laws,

773   the *I3ELVIS* code is able to model multiphase thermo-mechanical flow approximating ductile-

774   brittle deformation of rocks for long time scales.

775

776   *Fluid/melt dynamics: dehydration, fluid transport, partial melting and melt extraction*

777   *computing*

778   In our experiments, each defined lithology can be dry or hydrated, with pressure- and

779   temperature-dependent stable mineralogical water content. Additional porous water content

780   X_{H2O} (wt.%) is prescribed in the sediments and hydrated oceanic crust and decreases linearly

781   from the surface to 75 km depth mimicking the effects of low-temperature reactions:

782      $$X_{H_2O} = X_{H_2O(0)} \left(1 - \frac{\Delta y}{75}\right) \tag{5}$$

783   where Δy is the depth below the surface and $X_{H2O(0)}$ is the porous water content at the

784   surface [*Johnson and Pruis*, 2003]. During subduction, the local water content of hydrated

785   sediments and oceanic crust can exceed their maximum water content generating

786   independently moving water markers in the mantle wedge. The 3D velocity of these markers

787   is then solved according to pressure gradient [*Faccenda et al.*, 2009]:

788    $$V_{x(water)} = v_x - A \frac{\partial p}{\partial x}$$

789    $$V_{y(water)} = v_y - A \left(\frac{\partial p}{\partial y} - g \, \rho_{fluid} \right)$$ (6)

790    $$V_{z(water)} = v_z - A \frac{\partial p}{\partial z}$$

791   where ρ_{fluid} is the fluid density and *A* is the water percolation constant calculated as:

792    $$A = \frac{v_{percolation}}{g \, (\rho_{mantle} - \rho_{fluid})}$$ (7)

793   where $v_{percolation}$ is the presumed standard water percolation velocity in the mantle

794   [*Nikolaeva et al.*, 2008] and ρ_{mantle} is the mantle density. Mobile water is then absorbed by the

795   surrounding mantle or crustal rocks by hydration process depending on pressure, temperature

796   and rock composition (see details in [*Zhu et al.*, 2013]).

797   Partial melting process is also included in our experiments and the volumetric melt fraction

798   is calculated for all rocks, excepted hydrated mantle, as:

799    $$M_0 = 0 \quad \text{at } T < T_{solidus}$$

800    $$M_0 = \frac{T - T_{solidus}}{T_{liquidus} - T_{solidus}} \quad \text{at } T_{solidus} < T < T_{liquidus}$$

801   (8)

802    $$M_0 = 1 \text{ at } T > T_{liquidus}$$

803   where M_0 is the volumetric fraction of melt with no previous melt extraction, $T_{solidus}$ and

804    $T_{liquidus}$ are, respectively, the solidus and liquidus temperatures depending on the pressure and

805   rock composition (Table S1). For the hydrated mantle, the degree of partial melting also

806   depends on the water content according to the parameterization of *Katz et al.* [2003] that is

807   constrained by thermodynamic experimental modeling. Resulting partially molten rocks can

808   then undergo a succession of melt extraction episodes depending on their melt extraction

809   threshold M_{max} and non-extractable melt fraction M_{min}, both equal to 1 %. Only the exceeding

810   volumetric melt fraction (i.e. > 1 %) is then extracted from partially molten rocks and tracked

811   by partially molten rock markers. For each extraction episode, the melt fraction M_{ext} recorded

812   in the partially molten rock markers is calculated as:

813 $$M_{ext} = M - M_{min} \tag{9}$$

814   where M is the volumetric melt fraction in partially molten rock which accounts for

815   previous extraction episodes and is calculated as:

816 $$M = M_0 - \sum M_{ext} \tag{10}$$

817   where $\sum M_{ext}$ is the total melt fraction from previous extraction episodes. M varies then

818   dynamically (Eqs. 8 and 10) until remaining solid rock is considered as refractory (i.e. unable

819   to undergo additional partial melting) when $\sum M_{ext} > M_0$. Partially molten rock markers

820   resulting from these extraction episodes are then instantaneously transmitted to the surface as

821   free melt is assumed to propagate upward much faster than rocks deform [*Hawkesworth*,

822   1997]. At the surface, these markers create volcanic rocks characterized by their volume and

823   composition (i.e. partially molten source).

824

825   ***Rock properties and rheology***

826   The physical properties of rocks used in our experiments are given in Table S1. Among

827   them, the density of solid rocks ρ_{solid} is calculated as:

828 $$\rho_{solid} = \rho_{0solid} \left(1 - \alpha \left(T - 298\right)\right) \left(1 + \beta \left(p - 0.1\right)\right) \qquad (11)$$

829 where ρ_{0solid} is the standard density of solid rocks and α and β are respectively the thermal

830 expansion and compressibility of rock. For partially molten rocks, their effective density ρ_{eff} is

831 calculated as:

832 $$\rho_{eff} = \rho_{solid} \left(1 - M + M \frac{\rho_{0molten}}{\rho_{0solid}}\right) \qquad (12)$$

833 where $\rho_{0molten}$ is the standard density of molten rock. Non-Newtonian visco-plastic

834 rheologies used in our experiments are implemented by both ductile and brittle/plastic

835 experimentally constrained laws. Thus, the effective viscosity for dislocation creep depending

836 on the strain rate, pressure and temperature is calculated as:

837 $$\eta_{creep} = \dot{\varepsilon}_{II}^{\frac{1-n}{n}} A_D^{\frac{-1}{n}} exp\left(\frac{E + P\,V}{n\,R\,T}\right) \qquad (13)$$

838 where $\dot{\varepsilon}_{II}$ is the second invariant of the strain rate tensor, n (creep exponent), A_D (pre-

839 exponential factor), E (activation energy) and V (activation volume) are experimentally

840 determined parameters specific to applied viscous flow law (i.e. wet quartzite, plagioclase

841 (An$_{75}$), dry olivine and wet olivine flow laws; Table S1) [*Ranalli*, 1995]. R is the gas constant.

842 This ductile behavior is limited with a brittle/plastic one, implemented by using the Drucker-

843 Prager criterion σ_{yield} (i.e. plastic strength) [*Ranalli*, 1995] as:

844 $$\eta_{creep} \leq \frac{\sigma_{yield}}{2\,\dot{\varepsilon}_{II}} \qquad (14)$$

845 where σ_{yield} is calculated as:

846 $$\sigma_{yield} = c + p\,\sin(\varphi) \qquad (15)$$

847   where c is the cohesion of the rock and φ is the effective internal friction angle depending

848   on the fluid and melt contents (see details in *Gerya and Meilick* [2011]). The lower and upper

849   cut-off values for the viscosities of all rock compositions in our numerical experiments are

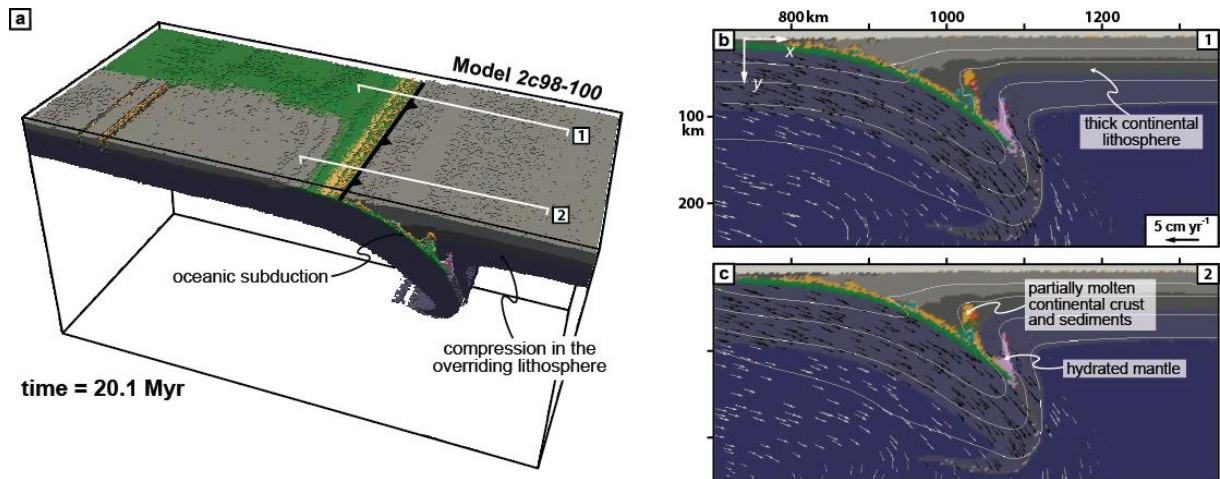850 10^{19} and 10^{24} Pa s, respectively.

851

Supplementary figures

853
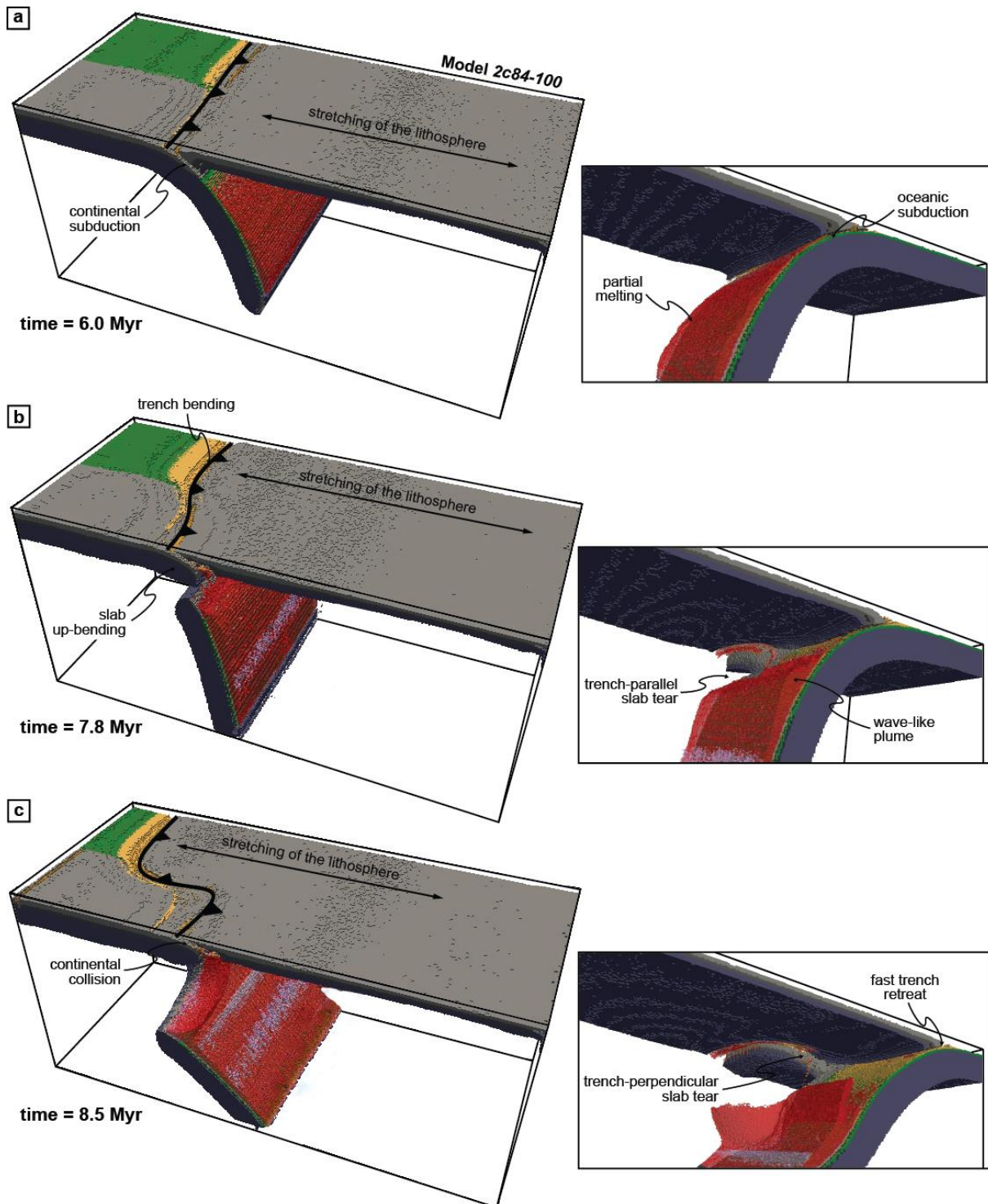
**Fig. S1:** Evolution of the model *2c84-100*. a, b, c) 3D lateral view of the subduction zone (left panels) and zoom on the mantle wedge (right panels) for selected time steps. Colors represent the different rock types (see Fig. 4 for detailed legend). Asthenosphere and other phases are cut off for clarity.

858

859

Fig. S2: Subduction geometry of the model *2c98-100* displaying a relatively strong coupling between both interacting lithospheres. a) 3D lateral view of the subduction zone highlighting the compressional tectonics in the overriding continental lithosphere. b, c) *x-y* cross-sections of the subduction zone highlighting the restrained magmatic activity in the mantle wedge and the low velocity field in both the subducting lithosphere and the underlying asthenosphere (see Fig. 4 for detailed legend).

865
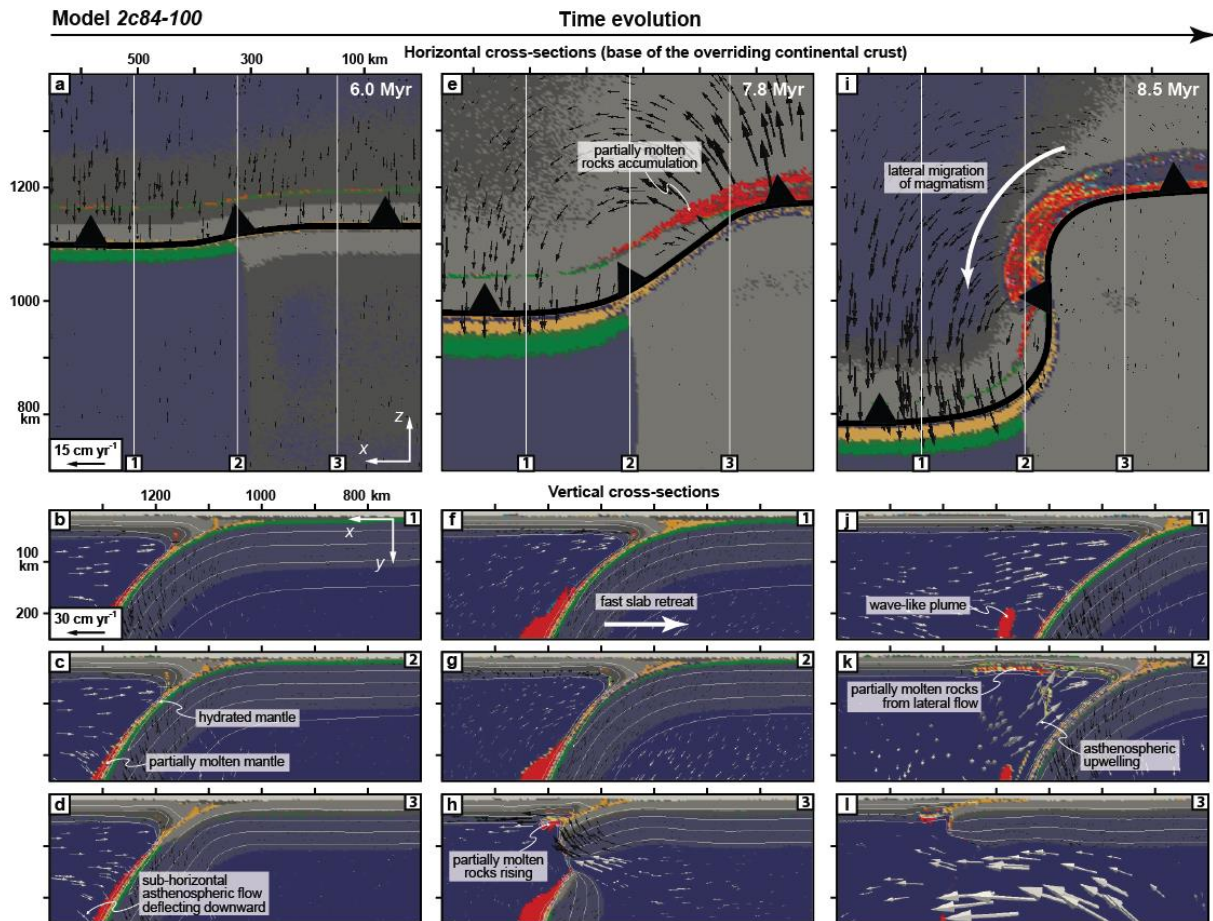
Fig. S3: Evolution of magmatism in model *2c84-100*. *x-z* plan views (a, e, i) and *x-y* cross-sections (b, c, d, f, g, h, j, k, l) of the subduction zone for selected time steps. Colors represent the different rock types (see Fig. 4 for detailed legend). Black and white arrows represent velocity vectors in the continental crust (top panels) or lithospheric mantle (bottom panels) and the asthenosphere, respectively. Scale of velocity vectors is twice larger in top panels than in bottom panels. White lines (bottom panels) represent 300, 600, 900 and 1200 °C isotherms.

874 **Supplementary tables**

875

Material	Density ρ_0	Isobaric heat capacity C_p	Thermal conductivity k	Radiogenic heat production H_r	$T_{solidus}$	$T_{liquidus}$	Thermal expansion α	Compres-sibility β	Viscous flow law	Creep exponent n	Activation energy E	Activation volume V
	(kg m-3)	(J kg^{-1} K^{-1})	(W m^{-1} K^{-1})	(mW m^{-3})	(K)	(K)	(K^{-1})	(MPa^{-1})			(kJ mol^{-1})	(cm^3 mol^{-1})
Air	1	100	20	0			0	0	Air	1	0	0
Sea water	1000	3330	20	0			0	0	Water	1	0	0
Sediments	2600 (solid) 2400 (molten)	1000 1500	0.64+807/(T-77)	2	889+179/(P+54)+20200/(P+54)² at P < 1200 MPa; 831+0.06P at P > 1200 MPa	1262+0.09P	3×10^{-5}	3×10^{-3}	wet quartzite	2.3 1	154	0
Upper continental crust	2750 (solid) 2700 (hydrated) 2400 (molten)	1000 1500	0.64+807/(T-77)	1	889+179/(P+54)+20200/(P+54)² at P < 1200 MPa; 831+0.06P at P > 1200 MPa	1262+0.09P	3×10^{-5}	3×10^{-3}	wet quartzite	2.3 1	154 0	0
Lower continental crust	2950 (solid) 2900 (hydrated) 2400 (molten)	1000 1500	0.64+807/(T-77)	0.5	1327.15+0.0906P	1423+0.105P	3×10^{-5}	3×10^{-3}	wet quartzite	3.2 1	238 0	0
Oceanic crust	3000 (solid) 3000 (hydrated) 2900 (molten)	1000 1500	1.18+474/(T-77)	0.25	1327.15+0.0906P 973-70400/(P+54)+778×10^5/(P+354)² at P < 1600 MPa; 935+0.0035P+6.2×10^{-6} at P > 1600 MPa	1423+0.105P	3×10^{-5}	3×10^{-3}	Plagiocalse (An$_{75}$) wet quartzite Plagiocalse (An$_{75}$)	3.2 2.3 1	238 154 0	0
Mantle	3300 (solid) 3300 (hydrated/ serpentinized) 2900 (molten)	1000 1500	0.73+1293/(T-77)	0.022	n/a P-T-H_2O dependent melting model of Katz et al. (2003)	n/a	3×10^{-5}	3×10^{-3}	dry olivine wet olivine dry olivine	3.5 4 1	532 470 0	0.8
Weak zone	3300	1000	0.73+1293/(T-77)	0.05	n/a	n/a	3×10^{-5}	3×10^{-3}	wet olivine	4	470	0.8

876

877 **Table S1:** Material properties used in the numerical experiments. See details in the text.

878

Models with two-layer continental crust		thermal age of the oceanic lithosphere			
		40 Ma	60 Ma	80 Ma	100 Ma
depth of the 1300 °C isotherm in the overriding lithosphere	84 km	2c84-40	2c84-60	2c84-80	**2c84-100**
	89 km	2c89-40	**2c89-60**	2c89-80	2c89-100
	93 km	2c93-40	2c93-60	2c93-80	2c93-100
	98 km	2c98-40	2c98-60	2c98-80	**2c98-100**

879

880

Models with one-layer continental crust		thermal age of the oceanic lithosphere		
		60 Ma	70 Ma	80 Ma
depth of the 1300 °C isotherm in the overriding lithos.	111 km	1c111-60	1c111-70	1c111-80
	113 km	1c113-60	**1c113-70**	1c113-80
	115 km	1c115-60	1c115-70	1c115-80

881 **Table S2:** Range of performed models with variations in the continental crust structure and
882 geothermal gradient in the continental and oceanic lithospheres leading to explore the role of
883 lithosphere rheology on subduction dynamics and magmatic evolution. The overriding lithosphere in
884 dark grey, light grey and white models undergoes, respectively, a compressional, minor extensional
885 and major extensional tectonics. Models in bold are described in the text.

886